Study of the FCC+L12 two-phase region in complex concentrated alloys based on the Al-Co-Cr-Fe-Ni-Ti system

T. Rieger, J.-M. Joubert, M. Laurent-Brocq, L. Perrière, I. Guillot, J.-P. Couzinié

Study of the FCC+$L1_2$ two-phase region in complex concentrated alloys based on the Al–Co–Cr–Fe–Ni–Ti system

Rieger T., Joubert J.-M., Laurent-Brocq M., Perrière L., Guillot I. and Couzinié J.-P.*

Université Paris Est Creteil, CNRS, ICMPE, UMR7182, F-94320, Thiais, France

* corresponding author. *E-mail address*: couzinie@icmpe.cnrs.fr

Keywords: High entropy alloys, Thermodynamic stability, Calphad approach, Precipitation, $L1_2$ phase

Abstract

New face-centered cubic (FCC) multicomponent alloys designed through the high-entropy (HEA) concept and strengthened with $L1_2$ ordered precipitates are promising material solutions for high temperature (HT) structural applications. However, as the design strategy is based on multi-principal elements, the research of alloy compositions exhibiting a stable and well-controlled FCC+$L1_2$ microstructure at HT is particularly challenging. Among the critical issues, those relative to the extent and the stability of the FCC+$L1_2$ two-phase region in the wide compositional space have to be addressed. Here, we performed high-throughput Calphad calculations in the senary Al–Co–Cr–Fe–Ni–Ti system in the 800°C-1000°C range to screen alloy compositions exhibiting duplex FCC+$L1_2$ microstructures. From the 79 695 analyzed compositions, we show that roughly 6% of the total own duplex microstructure at 800°C and 1000°C. Calculations suggest that Cr and Fe additions destabilize the two-phase region. Interestingly we found that Fe is a good candidate to substitute Co or Ni in the FCC phase and potentially induce some solid solution strengthening effects. Finally, the present results allow to propose an original 2D visualization method of the two-phase FCC+$L1_2$ region in the complex compositional space. The method is based on the relative influence of the alloying elements on the formation of such microstructure. To assess the reliability of calculations, six alloys were designed and characterized. A good agreement is found between predictive calculations and experimental results except for Cr- and Al-free alloy compositions in the quaternary Co–Fe–Ni–Ti system, due to the absence of description of the τ phase with $(Ni_{0.5}Co_{0.5})_3Ti$ composition in the selected thermodynamic database.

1. Introduction

Progress in high social impact fields relies on the development of new materials solutions with enhanced functional and/or structural properties. Beyond the incremental improvements of existing solutions, new alloy design strategies have emerged. Among the most attractive recent approaches, the one based on the mixing of multi-principal base elements has paved the way for 15 years and has led to the study and the development of new complex materials, so called high entropy alloys (HEAs). Initially motivated by the idea to explore central parts of phase diagrams or to produce concentrated solid solutions by maximizing the configurational mixing entropy of the system [1,2], the concept offers a breakthrough in the approach of alloy design [3]. The initial high-entropy concept as developed by Yeh *et al.* revisits the whole notion of alloying, with the initial motivation to design multi-component metallic materials with single-phase solid solutions.

The first generation of HEAs has received much attention in the past 10 years and has been mainly focused on two families: alloys based on 3d transition metals which often display face centered cubic (FCC) crystal structures [4,5] and alloys based on refractory elements with body-centered cubic (BCC) microstructures [6–8]. The development of the first family has been relied on the quinary equiatomic CoCrFeMnNi composition (Cantor alloy [1] and its derivatives [4]) which has gained great interest from the materials science community due to its excellent strength-ductility trade-off compared to other single-phase conventional alloys [9]. In the Co–Cr–Fe–Mn–Ni system, the Cantor alloy has been the most extensively studied [10–15]. It forms a “model” of true FCC solid-solution down to the atomic scale [16] and it is now proved that the FCC domain extends widely in the quinary system [17]. The equiatomic composition offers attractive mechanical properties [10,18,19]: it displays a temperature independent fracture toughness up to 200 $MPa.m^{1/2}$ and also an unusual mechanical behavior with an increase of both strength and ductility with decreasing temperature [14,19–21]. This alloy and its single-phase derivatives are considered as potential attractive candidates for structural applications. However, concentrated FCC solid solutions retain – in many cases – limited mechanical properties for temperatures up to 800°C, with yield strengths close to 100 MPa and ultimate tensile strengths down to 200 MPa [10]. Those numbers are far from many requirements, especially if one considers structural applications in aerospace industry [22]. New microstructures are thus required to significantly improve high temperature (HT) mechanical properties of the concentrated alloys.

In this specific context, the high entropy alloy concept offers tremendous opportunities. Among the avenues being explored, the addition of elements in the multi-principal base elements aimed at producing secondary strengthening phases seems to be the most reliable solution. Such a strategy is yet challenging due to the chemical complexity of the systems: alloy chemistry must be controlled to achieve the adequate precipitation (nature of the phases, volume fraction, size of particles) whilst avoiding the potential formation of phases with detrimental effects on mechanical properties. Indeed,

precipitation of intermetallic phases such as σ, μ, Laves, $L2_1$, B2 and $L1_2$ were observed in many FCC complex concentrated alloys (CCAs), competing with the entropy-stabilized solid solution [23,24]. Whereas σ and Laves phases are brittle and undesirable for HT applications, ordered B2 and $L1_2$ phases appear as ideal candidates to harden the complex concentrated solid solutions. The B2 phase appears by adding Al in FCC Co–Cr–Fe–(Mn)–Ni systems [25]. The impact of the heterogeneous precipitation of the B2 phase on the yield strength could be significant at room temperature, as recently evidenced by Dasari *et al.* in the $Al_{0.5}Co_{1.5}CrFeNi_{1.5}$ composition [25]. However, reports on the effect of such precipitation on the mechanical properties of CCAs at HT are missing. On the contrary, the precipitation of the $Ni_3(Al,Ti)$-$L1_2$ ordered phase has recently gathered a great interest in FCC HEA systems [26–45] (for a review, see [46]). As for Ni-based superalloys, the ordered phase is achieved in HEAs/CCAs by minor additions of Al and Ti. Additional elements have sometimes been incorporated with the aim of stabilizing the ordered precipitates (Cu) [47] or increasing the solvus temperature of the $L1_2$ phase (Nb) [44]. As initially expected, the presence of the coherent $L1_2$ precipitation is an efficient way to achieve an interesting balance between strength and ductility [26–31]. In addition, the evidence of an exceptional thermal stability of the strengthening phase in the concentrated FCC solid solution is promising for the future development of such materials solutions [36]. Moreover, recent research on HEAs/CCAs points out the beneficial effects of the strengthening phase on the HT mechanical properties [31,35,43,44].

Nevertheless, reported studies have shown that a well-controlled duplex FCC+$L1_2$ microstructure is difficult to achieve in HEAs/CCAs [26,42,44]. Multiple precipitation is often observed in these systems with a possible negative impact on the HT mechanical properties [48]. The extent of the FCC+$L1_2$ phase domain is rather limited (temperature and composition ranges) when minor additions of Al and Ti are introduced in (FCC) equiatomic single phase Co–Cr–Fe–Ni base alloys and low volume fractions of the strengthening phase are generally observed (<20%) [49,50]. Hence, some efforts on alloying design are required to optimize crucial microstructural parameters and improve HT resistance of strengthened FCC HEAs/CCAs. To this aim, and from the recent studies in the field, the different alloying strategies used to define nominal compositions are mainly based on an incremental approach with thermodynamic predictions of phase equilibrium. Such an approach has led to the design and the study of strengthened FCC alloys with dominant base compositions departing from the equimolar one, for instance in the Al–Co–Cr–Fe–Ni–Ti [40,44,51] and Al–Co–Cr–Cu–Fe–Ni [42] systems. If properly controlled, such a deviation from equiatomic proportions may lead to an increase of the volume fraction of $L1_2$ phase giving rise to attractive HT properties [44]. However, there is currently no in-depth study aimed at mapping and studying the peculiarities of the FCC+$L1_2$ two-phase region in the vast compositional space of the HEAs/CCAs [46].

In this context, the current research is focused on two main aspects. First, the detailed description of the two-phase region in the Al–Co–Cr–Fe–Ni–Ti senary system in the 800°C-1000°C temperature range is

performed using high-throughput thermodynamic calculations. The Calphad (CALculation of PHase Diagrams) method is chosen to screen the alloy space. Among the key issues, the thermodynamic study will try to address the following points:

- What is the extent of the duplex phase region in the Al–Co–Cr–Fe–Ni–Ti senary system at 800°C and 1000°C?
- Is there a reliable way to visualize the FCC+$L1_2$ phase region in the vast alloy compositional space?

Finally, the design and the study of six complex alloys with FCC+$L1_2$ microstructure is conducted to assess the predictive character of calculations and propose potential new materials solutions for HT structural applications.

2. Methods

2.1. Calculation method

The prediction of phase equilibria in the Al–Co–Cr–Fe–Ni–Ti system has been performed using the Calphad approach. The method is based on the calculation of the equilibrium in given conditions by energy minimization done using a thermodynamic database in which the Gibbs energy of the phases are described using semi-empirical functions of temperature, pressure and composition. Binary and ternary systems are optimized on experimental, thermodynamic and DFT data. Higher order systems are then extrapolated.

Combined approaches/strategies have been proposed in the past few years to design HEAs and more particularly the systems able to form single solid solutions [52–55]. The approaches often use a combination of sophisticated tools which require a significant amount of experimental data which is yet difficult to get in the case of these new $L1_2$-strengthened HEAs [53,54]. The chosen methodology exclusively based on Calphad is close to that developed by Senkov and coworkers [52] or Bracq *et al.* [17] aimed at identifying equimolar alloy compositions with single solid solution microstructure and studying the phase stability of FCC solid solution in 3d metal transition based-alloys, respectively. We will show that such an approach is efficient in our study and that the Thermo-Calc database dedicated to HEAs (TCHEA3) is well-suited to predict FCC+$L1_2$ microstructure in the senary system. The database includes 26 elements and 438 phases and the Al–Co–Cr–Fe–Ni–Ti system is described with 105 phases originating from the 15 binaries and 20 ternaries. All binaries and 12 of the 20 ternaries have been assessed in full range of composition and temperature [56].

First, high-throughput calculations were carried out in the senary system to scan the area of interest in the compositional space and analyze its peculiarities. The TC-Toolbox for Matlab was used allowing loop programming of calculations and easy handling of results through multi-dimensional matrices.

The resolution in the compositional space was set as follows: the Cr–Co–Fe–Ni quaternary phase diagram was initially calculated using a step of 5 at.% for each element. Then, Al and Ti were added with a 2.5 at.% step up to [Al] + [Ti] = 20 at.%. The step in Co, Cr, Fe and Ni was continuously reduced from 5 at.% down to 4 at.% to balance the addition of Al and Ti. In this way, the same number of compositions (1771) was calculated for each given [Al] + [Ti] content. As much as 79 695 compositions were calculated at 800 and 1000°C with 45 combinations of [Al] and [Ti].

Along with these calculations, the visualization of the FCC+$L1_2$ domain in the senary system has been carried out. The approach has been developed to represent the different nominal alloy compositions, their associated equilibrium phases, the $L1_2$ solvus and the solidus temperatures in a two-dimensional perspective. Such a methodology has required two steps. First, the Al–Co–Ni–Ti quaternary phase diagram was calculated. This system is a key element in the current study since two $L1_2$ phases originate from the Ni–Al and Co–Ti binaries [57]. Calculations were performed at 800°C with a 1 at.% step and [Al] + [Ti] ≤ 30 at.%. A perspective of the FCC+$L1_2$ region is then developed considering sections of the quaternary phase diagram with fixed [Al] + [Ti]. Finally, multiple sections are created with the addition of Cr and Fe which substitute Co and Ni. 441 (21x21) alloy compositions form each individual section. Calculations were performed considering a 5 at.%. step for [Cr] and [Fe] additions and up to [Cr] + [Fe] ≤ 55 at.%. 78 sections were required to target the desired compositional space. Three temperatures were used in the study: 800°C, 900°C and 1000°C for a total of 103 194 equilibrium calculations.

Room temperature (RT) alloy density has been computed using the FCC and $L1_2$ phase fractions and compositions at 900°C with molar volumes computed at RT.

2.2. Experimental methods

A total of six alloys, TA1 to TA6, were processed. Chemical compositions are given in Table 1.

Alloys were prepared using high frequency induction melting of raw elements of at least 99.5 wt.% purity. The melting process was carried out in a water-cooled copper crucible under He atmosphere followed by gravity casting to shape the ingots into 13 mm diameter rods. These rods were then cut into 12 mm high cylinders.

Subsequently, TA1 to TA5 cast alloys were wrapped in tantalum sheets and put through a staged annealing process in a sealed silica tube filled with argon. Alloys were introduced into a furnace at 1150°C and maintained at this temperature during 48h to ensure chemical homogeneity. They were then cooled down to 900°C at a cooling rate of 10°C/min and maintained at this temperature for 403h to achieve thermodynamic equilibrium before water quenching.

X-ray diffraction (XRD) was carried out with a PANalytical XPert Pro diffractometer using the Co-Kα radiation at a wavelength of 0.178897 nm. Le Bail (pattern matching) refinement was finally used to determine lattice parameters using FullProf software [58].

Scanning Electron Microscopy (SEM) examination was performed with samples that were hot mounted in a conductive resin and prepared by mechanical grinding using 320 to 4000 grit SiC papers followed by a final polishing step using a vibratory table and a 0.04 mm colloidal silica for 2h. A field emission gun Merlin Zeiss SEM was used. Average chemical compositions have been measured using energy dispersive spectroscopy (EDS). Two maps were recorded at very low magnification (30x) for each sample. Volume fractions were determined from a total of twenty back-scattered electrons (BSE) pictures automatically analyzed with the ImageJ software. Reported experimental fractions are the average of the twenty measurements with uncertainties in a 95% confidence interval.

Transmission electron microscopy (TEM) samples were grinded into discs of 3 mm in diameter and 100 µm thick. Thin foils were then electropolished using a twin-jet Tenupol-5 with a 10% $HClO_4$ solution in methanol at 20 V and -35°C. Observations were performed using a JEOL2000EX and a field emission gun FEI Tecnai F20.

Differential scanning calorimetry (DSC) was performed using a Netzsch 404 heat-flux calorimeter with a heating rate of 10°C/min up to 1400°C under an Ar atmosphere allowing to determine the solidus, liquidus and $L1_2$ solvus temperatures of the alloys. Samples were cut and grinded into 1 mm thick parallelepipeds weighing approximately 75 mg. The transition temperatures were determined at the onset of the corresponding peaks. To ensure reproducibility, two samples of each alloy were tested. The given transition temperatures are the average of these two measurements.

The density measurements were carried out by hydrostatic weighing in distilled water. Five measurements were carried out for each sample and the given uncertainties are the 95% confidence interval.

3. Results

3.1. CALPHAD Calculations

3.1.1. High-throughput calculations

79 695 alloy compositions were computed at 800°C and 1000°C considering Co, Cr, Fe and Ni from 0 to 100 at.% and Ti and Al from 0 to 20 at.% with [Al] + [Ti] ≤ 20 at.%. An alloy composition was considered with a duplex FCC+$L1_2$ microstructure if the following criteria were met: [FCC] + [$L1_2$] > 99%, [FCC] > 1% and [$L1_2$] > 1% at 800°C and 1000°C, where [X] is the molar fraction of the X phase. Among the 79 695 computed compositions, 7 617 and 5 878 are FCC+$L1_2$ at 800°C and

1000°C, respectively. As much as 4 562 compositions own duplex microstructure at both temperatures which is roughly 6% of the entire calculated domain.

Each alloying element of the senary system plays a key role on the extent of the FCC+$L1_2$ domain in the compositional space and can be analyzed by assessing the ratio of FCC+$L1_2$ compositions (*i.e.* alloy compositions exhibiting FCC+$L1_2$ microstructure) at both temperatures for a given concentration interval (Fig. 1). This ratio will hereafter be referred to as two-phase ratio and is given for an [A,B[interval in (1).

$$(two-phase\ ratio)_{[A,B[} = \frac{(number\ of\ FCC{+}L1_2\ compositions)_{[A,B[}}{(number\ of\ calculated\ compositions)_{[A,B[}} \quad (1)$$

Three sub-groups are distinguished in the senary system: Ni and Co (Fig. 1a,b), Cr and Fe (Fig. 1c,d), Al and Ti (Fig. 1e,f).

The (Ni,Co) and (Al,Ti) sub-groups appear to be favoring the formation of FCC+$L1_2$ microstructures with an increasing two-phase ratio up to a threshold (Fig. 1a and 1e). On the contrary, the (Cr,Fe) sub-group looks less favorable, the ratio is maximized in Cr- and Fe-free alloys but decreases in the whole compositional space and no longer exists for [Cr] + [Fe] > 45at.% (Fig. 1c). The decrease is more pronounced for Cr than for Fe. These latter tendencies are even more apparent when the sum of the grouped elements is plotted (Fig. 1b, 1d, 1f). In the (Ni,Co) sub-group, Ni is the most effective addition element to produce a FCC+$L1_2$ microstructure since the ratio approaches 30% in the [70%-80%[range. A threshold value is established for [Ni] + [Co] = 40 at.% indicating the absence of a FCC+$L1_2$ domain for alloy compositions with [Ni] + [Co] < 40 at.% (Fig. 1b). The optimum is reached in the [Ni] + [Co] interval of [70%,80%[.

Likewise, Al and Ti additions favor the formation of the two-phase region (Fig. 1e). Ti seems to be more favorable than Al to get the desired FCC+$L1_2$ microstructure for compositions higher than 7.5 at.%. The maximum of the two-phase ratio is achieved for [Al] + [Ti] = 12.5 at% (Fig. 1f). The tendency is confirmed in Fig. 2 which gives a deeper insight into the repartition of the FCC+$L1_2$ compositions with Al and Ti additions. Whereas a limited number of compositions gives duplex microstructures when Al and Ti are added distinctly, the highest number of FCC+$L1_2$ compositions is achieved for joint addition of Al and Ti. The most favorable combination is found for [Al] = 5 at.% and [Ti] = 7.5 at.% (Fig. 2).

Results of the alloying elemental partitioning in the FCC+$L1_2$ compositions was evaluated and are given in supplementary materials.

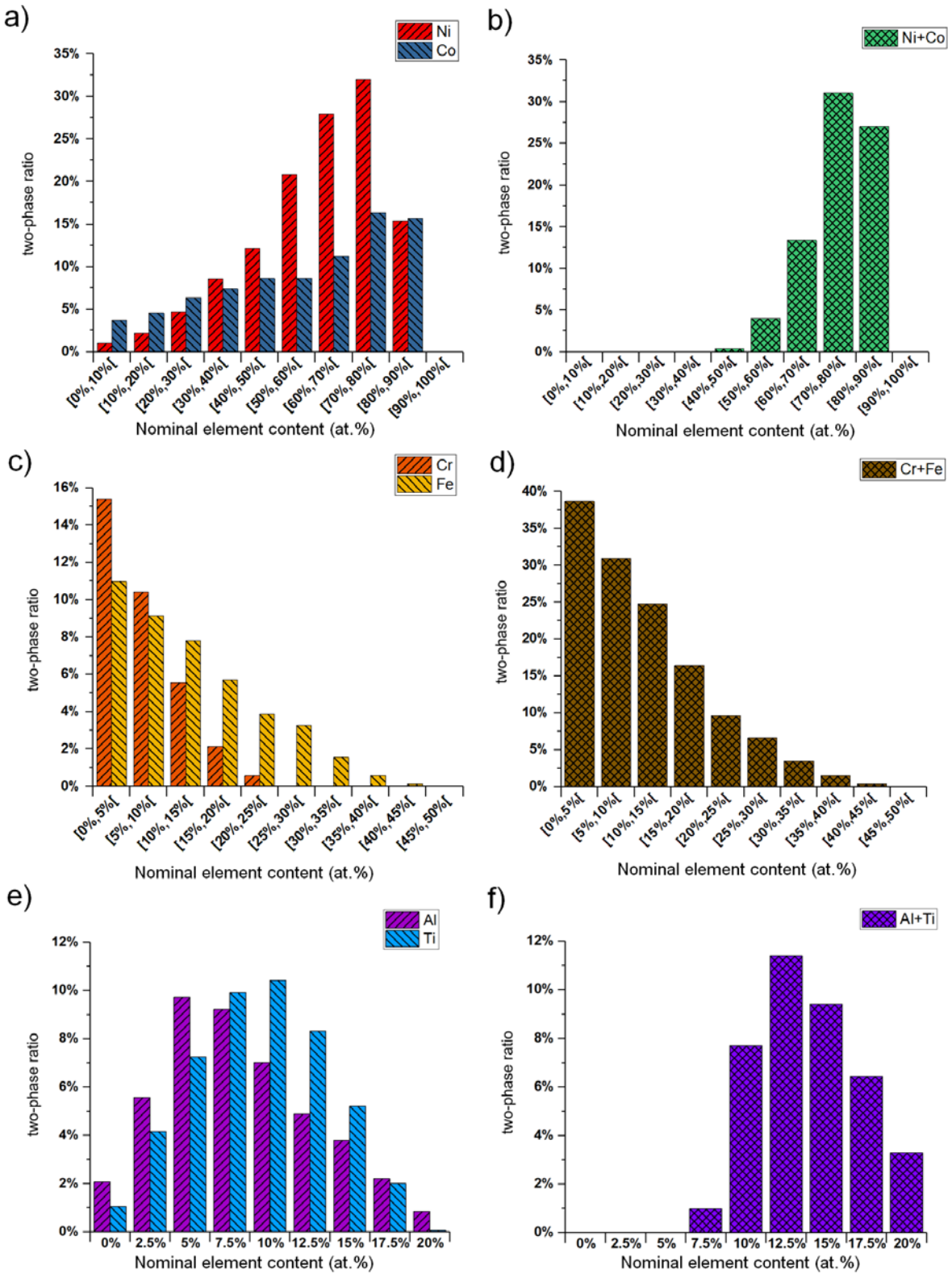

Figure 1: Proportion of alloy compositions exhibiting an FCC+$L1_2$ microstructure at both 800°C and 1000°C and for given concentration intervals: (a) Ni and Co, (b) Ni+Co sum, (c) Cr and Fe, (d) Cr+Fe sum, (e) Al and Ti, (f) Al+Ti sum.

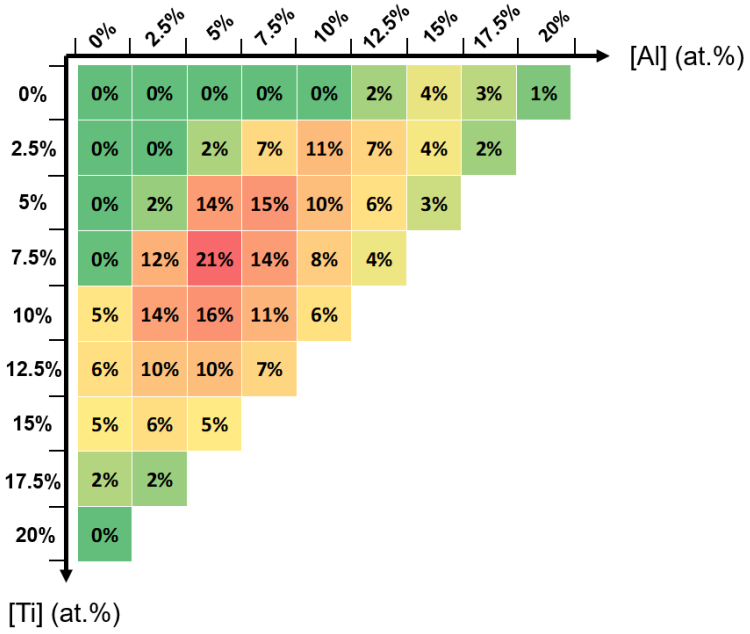

Figure 2: Repartition of the 4 562 alloy compositions with calculated FCC+$L1_2$ microstructure in the Al–Co–Cr–Fe–Ni–Ti system at both 800°C and 1000°C with Al and Ti concentration, irrespective of Co, Cr, Fe and Ni content. For a given Al and Ti content, the two-phase ratio of the 1 771 computed compositions is highlighted.

3.1.2. Visualization of the FCC+$L1_2$ two-phase region

Data have been collected at 800°C and 1000°C (cf. 3.1.1) to isolate key features of the calculated FCC+$L1_2$ two-phase region in the Al–Co–Cr–Fe–Ni–Ti senary system. However, the seven-dimensional space composed of five compositional dimensions, the temperature and the $L1_2$ phase fraction is not simple to capture. A way to visualize the two-phase region is then needed to have a grasp at the subtleties of the system. Since neither Cr nor Fe are required to form the FCC+$L1_2$ two-phase structure (Fig. 1), we started the calculations with the Al–Co–Ni–Ti quaternary system.

3.1.2.1 Al–Co–Ni–Ti quaternary system

Two binary sub-systems of the Al–Co–Ni–Ti system contain a $L1_2$ ordered phase in the 800-1000°C range: Co-Ti with Co_3Ti and Ni-Al with Ni_3Al. Equilibrium calculations were carried out in the Al-Co-Ni-Ti system at 800°C and the extent of the phase domains was plotted in a tetrahedron (Fig. 3). A continuous $L1_2$ phase region is predicted between Ni_3Al and Co_3Ti as well as the FCC phase region between the Co and Ni vertices of the tetrahedron (Fig. 3). The two-phase region is also continuous and lies in-between the FCC and $L1_2$ regions from the FCC-$L1_2$ tie-line from the Ni-Al to Co-Ti systems.

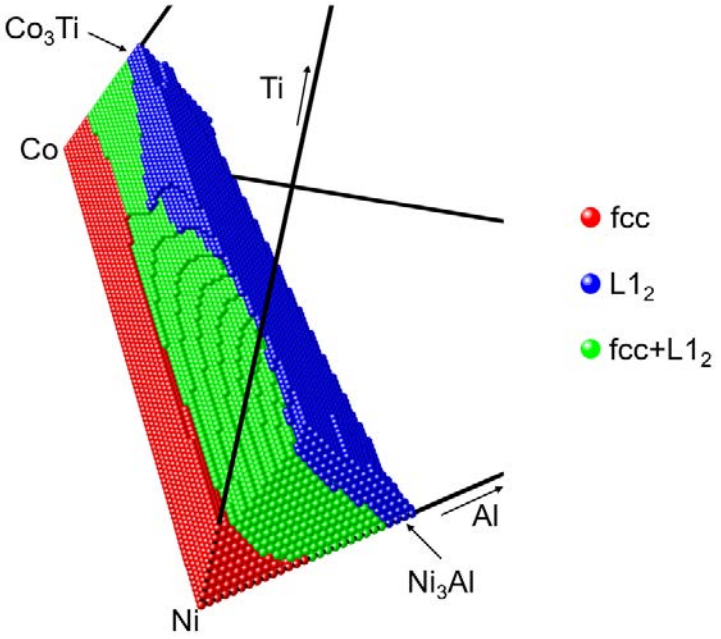

Figure 3: Representation of the Al–Co–Ni–Ti quaternary system calculated at 800°C. The FCC (red), $L1_2$ (blue) and FCC+$L1_2$ (green) regions are shown. The step used for calculations (also corresponding to one sphere in the figure) is 1at.%.

A two-dimensional perspective is however required to ease the visualization of the system in a broad range of alloy compositions. Thus, the representation of the FCC+$L1_2$ two-phase region will then be displayed along the direction defined by [Al] + [Ti] = x (x < 25 at.%). A fixed value of [Al] + [Ti] = 12.5 at.% was chosen as it corresponds to the amount for which the number of FCC+$L1_2$ compositions is the largest (Fig. 1f). Thus, a section of the Al–Co–Ni–Ti tetrahedron is featured (Fig. 4a). The corresponding FCC+$L1_2$ domain shown in figure 4b was obtained by combining calculations at 800°C, 900°C and 1000°C in such a way that only alloy compositions exhibiting (calculated) FCC+$L1_2$ microstructures at these three temperatures are evidenced. In this view, Al is linearly substituted by Ti along the x-axis and Co is linearly substituted by Ni along the y-axis (Fig. 4b). The $L1_2$ phase fraction at 800°C is evidenced using a color gradient.

3.1.2.2 Al–Co–Cr–Fe–Ni–Ti senary system

The projection of the dataset (4 562 computed alloy compositions exhibiting the appropriate microstructure at both 800°C and 1000°C) from the 6-dimensional space to a lower one has required a principal component analysis (PCA). The results of the analysis clearly show that the dataset is still highly spread along directions which correspond to the Co and Ni content of the alloy compositions (see supplementary material). Consequently, the representation adopted in 3.1.2.1 is maintained taking into account the presence of Cr and Fe. The available FCC+$L1_2$ compositions and the associated $L1_2$ fraction were plotted for different Cr and Fe content along [Al] + [Ti] = 12.5 at.% (Fig. 4c). A section with a given Cr and Fe content is plotted if at least one alloy composition exhibits an FCC+$L1_2$

microstructure. No FCC+$L1_2$ compositions were obtained for [Fe] ≥ 55 at.% and [Cr] ≥ 25 at.%. (Fig. 4c). The influence of Cr and Fe additions could be summarized as follows:

- the extent of the FCC+$L1_2$ domain is reduced whatever the addition of Cr and Fe;
- some $L1_2$-rich regions appear with the addition of Fe.

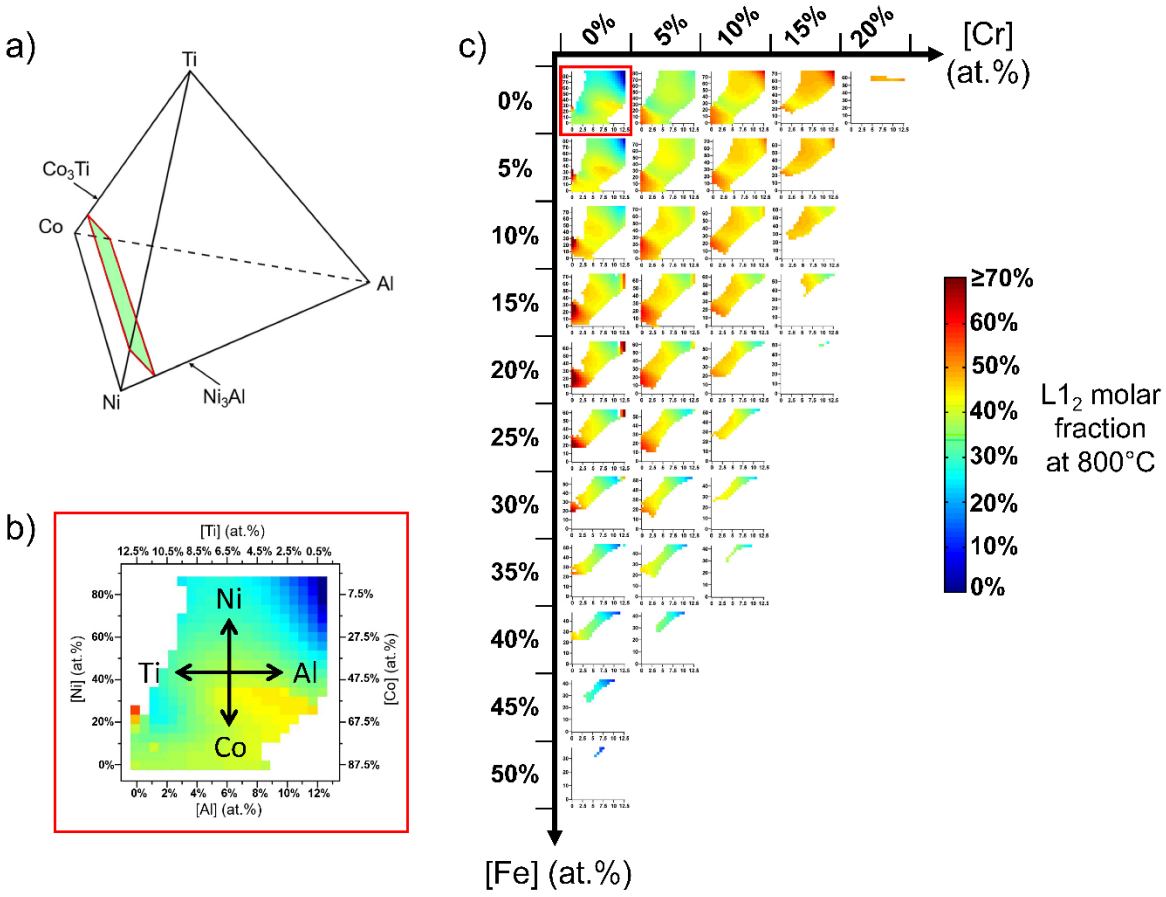

Figure 4: a) Section of the quaternary Al–Co–Ni–Ti phase diagram for [Al] + [Ti]=12.5 at.%, b) evolution of the $L1_2$ phase fraction with alloy composition at 800°C for the section displayed in a). Each point corresponds to a computed composition exhibiting a duplex microstructure (condition: [FCC] + [$L1_2$] > 99%) at 800°C, 900°C and 1000°C). c) same representation for [Al] + [Ti] = 12.5 at.% but for different Cr and Fe contents. Note that b) and c) share the same heat-map and also the same scale.

The increase of Cr or Fe content reduces the number of alloy compositions with FCC+$L1_2$ microstructures, especially in (Co,Al)-rich regions of the sections for which the B2 phase appears. Furthermore, the progressive addition of Fe reveals the presence of alloy compositions exhibiting high $L1_2$ phase fraction in the (Co,Ti)-rich corner ([Fe] < 35 at.%). The addition of Fe also ends up enhancing the $L1_2$ phase fraction in (Ni,Al)-rich regions up to a threshold ([Fe] = 25 at.%). Results on the Cr effect suggest the existence of a threshold between [Cr] = 15 at.% and [Cr] = 20 at.% after which the number of alloy compositions with duplex microstructure almost drops to zero.

The $L1_2$ solvus and solidus temperatures were computed for FCC+$L1_2$ compositions. Using the same representation of figure 4c), the mapping of these temperatures is given in figures S2 and S3, respectively. The $L1_2$ solvus temperature is highly correlated to the $L1_2$ fraction at 800°C. Cr and Fe have opposite influence on the $L1_2$ solvus temperature. Whereas Cr additions tend to increase the $L1_2$ solvus temperature, additions of Fe seems to lower it except in the (Co,Ti)-rich corner. The solidus temperature representation yields clear trends. Indeed, Ni-based compositions own higher melting points than Co-based compositions with a linear continuity between these two regions. At equivalent Ni/Co and Al/Ti ratios, the solidus temperature slightly decreases with additions of Cr and Fe.

The proposed representation enables the visualization of the extent of the equilibrium phases in the spreading direction of the FCC+$L1_2$ region, thus allowing to observe it in a wide range of compositions.

3.2 Experimental results

3.2.1. FCC+$L1_2$ compositions (TA1 to TA5)

The assessment of the approach has been established from the study of five alloys predicted with FCC+$L1_2$ microstructure in the 800-1000°C temperature range. TA1, TA2 and TA3 were designed using isopleths and Cr and Fe content for [Al] = [Ti] = 5 at.%. TA4 and TA5 were selected from the 79 695 computed compositions (cf. 3.1.1). The following selection criteria were considered:

- [Cr] ≥ 10 at.% for oxidation resistance.
- presence of a wide enough solution treatment window (FCC domain): $T_m - T_{L12} > 50$°C where T_m is the predicted melting temperature of the alloy and T_{L12} the predicted solvus of the $L1_2$ phase. Additional computations were made to ensure that this last criterion was met.

The five alloys were chosen to cover the wide range of available alloy compositions. The nominal compositions are given in table 1. TA1, TA2 and TA3 contain lower [Al] + [Ti] content (10 at.%) than TA4 and TA5 (12.5 at.%). TA4 and TA5 are designed to compare two different compositions but with the same concentration in elemental sub-groups ([Ni] + [Co] = 56.9 at.%, [Cr] + [Fe] = 30.6 at.%, [Al] + [Ti] = 12.5 at.%), TA4 being similar to Ni-based superalloys ([Ni] > 50 at.%) and TA5 fits within the original definition of HEAs given by Yeh *et al*. [2].

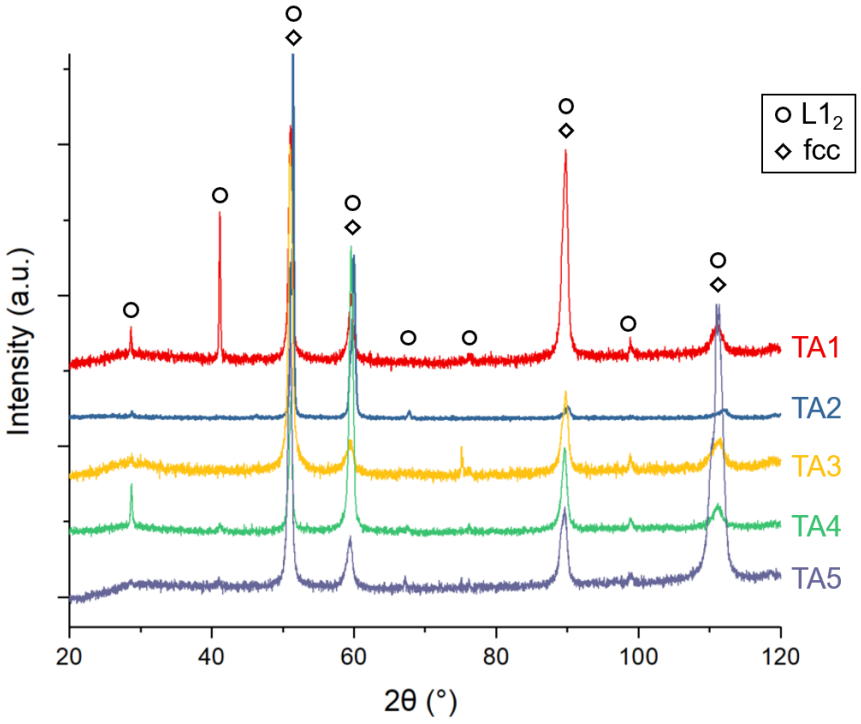

Figure 5: XRD measurements of TA1-TA5. The $L1_2$ reflections are indicated.

After heat treatments (1150°C/48h + 900°C/403h), XRD analysis showed that all five alloys featured an FCC structure with the presence of superlattice reflection peaks attributed to the $L1_2$ phase (Fig. 5). Duplex FCC+$L1_2$ microstructures were observed by SEM and TEM for all prepared alloys as predicted by the TCHEA3 database (Fig. 6 and Fig. S2). The five alloys exhibit a wide range of $L1_2$ precipitate morphologies. STEM-EDX mappings highlights the preferential partitioning of Al, Ni and Ti in the $L1_2$ precipitates as well as a depletion of Co, Cr and Fe as predicted by Calphad calculations (Fig. S2). The presence of some carbides and sulfides were also highlighted and related to the presence of impurities in raw materials.

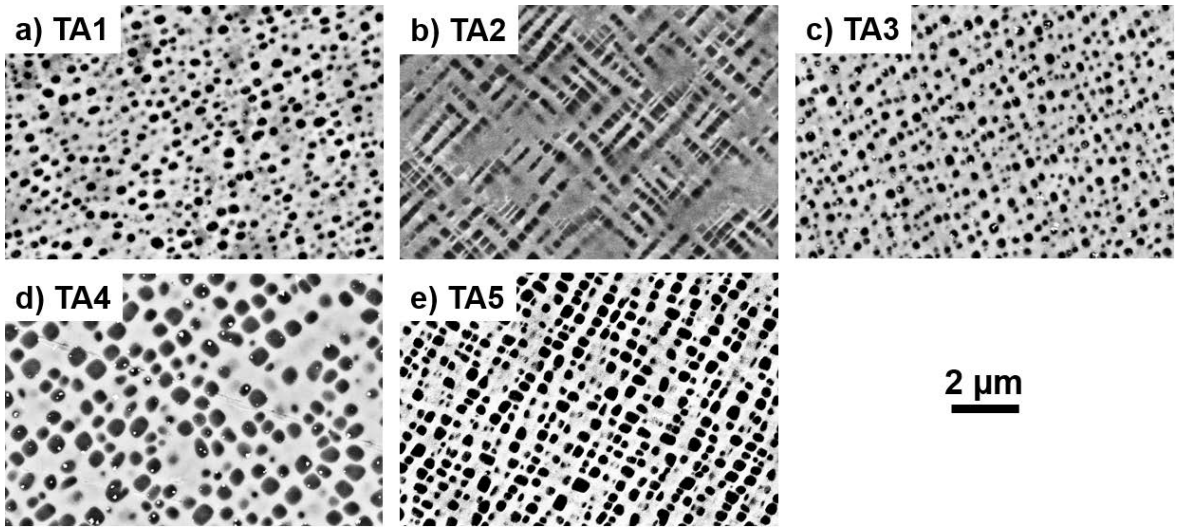

Figure 6: SEM-BSE micrographs of the FCC+$L1_2$ microstructure after heat treatments (1150°C/48h + 900°C/403h).

The $L1_2$ volume fractions predicted by the TCHEA3 database as well as the experimental values are given in table 1. A fairly good agreement is found except for TA3.

DSC was carried out for TA1 to TA5. Two endothermic peaks were visible during heating (Fig. S3). The first large peak close to 1000°C corresponds to the dissolution of the $L1_2$ phase [59] and gives the $L1_2$ solvus temperature. The second is observed for T > 1300°C and coincides with the melting of the alloy. Results are summarized in table 1.

Experimental transformation temperatures are consistent with thermodynamic calculations. The solidus temperature is generally found higher than the prediction (50-80°C) except for TA4 for which the solidus temperature is only 20°C higher. The agreement between experimental and predicted solvus temperatures is good at the exception of TA4 for which a difference of 50°C is found.

Table 1: Experimental and calculated data for annealed alloys (1150°C/48h + 900°C/403h). Calculated data were obtained with the TCHEA3 database. Chemical composition and lattice parameters were determined by SEM-EDS mappings and XRD, respectively. Experimental $L1_2$ volume fraction were measured with SEM images. Uncertainties correspond to a 95% confidence interval.

Alloy name	Composition (at.%)												Lattice parameters			$L1_2$ Volume fraction at 900°C (%)		Solvus temperature (°C)		Solidus temperature (°C)		Liquidus temperature (°C)		Density (g.cm^{-3})	
	Al		Co		Cr		Fe		Ni		Ti															
	Nominal	EDS	Nominal	EDS	Nominal	EDS	Nominal	EDS	Nominal	EDS	Nominal	EDS	a_{fcc} (nm)	a_{L12} (nm)	Misfit (%)	TCHEA3	SEM	TCHEA3	DSC	TCHEA3	DSC	TCHEA3	DSC	TCHEA3	Archimedes
TA1	5.0	5.1	16.7	17.0	16.7	17.2	16.7	17.0	40.0	38.9	5.0	5.0	0.3591	0.3607	0.44	29.0	20.6 ± 0.7	1060	1072	1241	1293	1347	1365	7.871	7.768 ± 0.004
TA2	5.0	5.1	35.0	35.1	10.0	10.2	10.0	10.1	35.0	34.4	5.0	5.1	0.3599	0.3618	0.53	24.8	22.1 ± 0.7	1051	1056	1273	1326	1379	1391	8.010	8.080 ± 0.004
TA3	5.0	5.0	25.0	25.2	20.0	20.5	10.0	10.2	35.0	34.1	5.0	5.0	0.3586	0.3598	0.34	30.1	17.7 ± 1.2	1075	1072	1228	1289	1355	1364	7.819	7.919 ± 0.003
TA4	7.5	7.7	4.4	4.5	13.1	13.5	17.5	17.6	52.5	51.6	5.0	5.1	0.3594	0.3607	0.39	35.5	34.5 ± 1.1	1072	1124	1264	1285	1326	1349	7.759	7.906 ± 0.002
TA5	5.0	5.1	21.9	22.0	13.1	13.4	17.5	17.7	35.0	34.2	7.5	7.6	0.3589	0.3602	0.36	39.8	29.3 ± 0.9	1094	1094	1167	1245	1309	1337	7.804	7.853 ± 0.002
TA6	-	-	37.5	37.3	-	-	25.0	25.1	25.0	24.8	12.5	12.8													

3.2.2. About the existence of predicted single-phase $L1_2$ alloy compositions

As exposed in §3.1.2.2, the increase of Fe content in Cr-free alloys lets appear the presence of alloy compositions in the (Co,Ni,Ti)-rich zone for which a single-phase $L1_2$ region is highlighted. The presence of such region of the Co–Fe–Ni–Ti quaternary is quite unexpected. In order to check the reliability of the predictions in this specific region, the $Co_{37.5}Fe_{25}Ni_{25}Ti_{12.5}$ (TA6) alloy was prepared and annealed at 1000°C during 6 days to reach thermodynamic equilibrium.

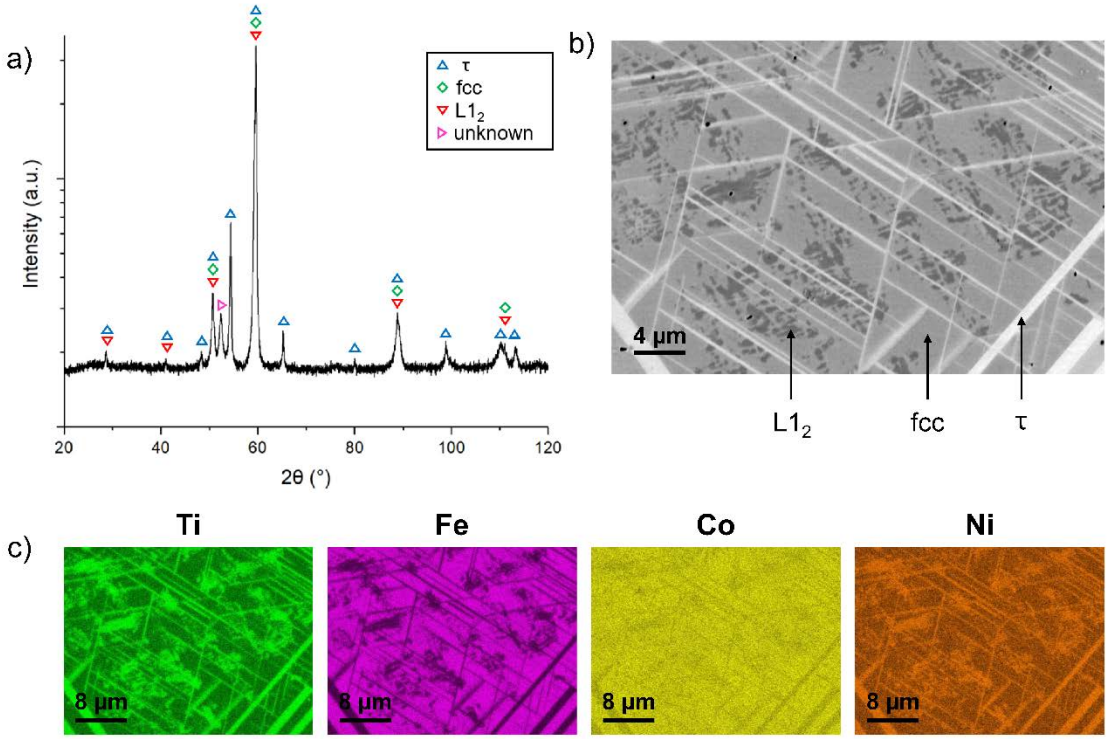

Figure 7: a) XRD pattern of TA6 alloy after 1000°C/144h annealing; b) SEM BSE picture and c) SEM-EDS elemental mapping.

TA6 is predicted to be $L1_2$ single phase above 900°C (Fig. S5) but XRD investigation highlights the existence of at least four phases (figure 7a): FCC, $L1_2$, Co_3V-type phase (so called τ) with $(Ni_{0.5}Co_{0.5})_3Ti$ composition and an unknown one. SEM observations confirm the multi-phased microstructure with the presence of platelets and globular Ni- and Ti-rich precipitates embedded in the matrix (Fig. 7b,c). The chemical compositions of the different phases analyzed by SEM-EDS are given in table 2.

Table 2: Chemical compositions of the phases observed in TA6 after heat treatment of 6 days at 1000°C and determined using SEM/EDS analysis (10 measurements). Uncertainties correspond to the standard deviation.

Phase composition (at.%)	**Co**	**Fe**	**Ni**	**Ti**
FCC	**39.0**	**31.4**	**20.7**	**9.0**
	± 0.2	**± 0.7**	**± 0.3**	**± 0.5**
$L1_2$	**35.5**	**14.4**	**30.9**	**19.2**
	± 0.7	**± 3.0**	**± 1.7**	**± 1.9**
τ	**33.4**	**9.4**	**34.9**	**22.3**
	± 0.1	**± 0.4**	**± 0.2**	**± 0.3**

4. Discussion

4.1. Comparison between experimental results and Calphad predictions

One of the objectives of the current study was to assess the predictive nature of the TCHEA3 database for candidate alloy compositions with FCC+$L1_2$ microstructures in the selected temperature target (800°C-1000°C). One critical requirement was to check the existence of a continuous $L1_2$ phase between Co_3Ti and Ni_3Al as experimentally reported [57,60]. This feature is accurately predicted by the TCHEA3 database (Fig. 3) and as the Al–Co–Ni–Ti quaternary phase diagram is a key part of the senary system, it appears reasonable to consider that the database is well suited for the description of the FCC+$L1_2$ region.

Six compositions were selected and suitable heat treatments were chosen in order to approach thermodynamic equilibrium. Evaluation of the database will be discussed based on the following points: equilibrium phases, volume fractions of $L1_2$ precipitates and transition temperatures.

Alloys can be divided into three categories: four senary CCAs with significant amount of Co (TA1, TA2, TA3 and TA5), one senary Ni-rich alloy (TA4) and one quaternary alloy in the Co–Fe–Ni–Ti system (TA6). Except for TA6, the processed alloys (TA1 to TA5) all featured a duplex FCC+$L1_2$ microstructure in accordance with Calphad predictions. However, our results highlight noticeable differences between experimental data and calculated ones. Thus, the predicted volume fractions (Vf) of the $L1_2$ phase are slightly overestimated with relative differences defined as $|Vf_{measured}-Vf_{predicted}|/Vf_{predicted}$ (Table 1): 10% for TA1, TA2, TA5 to 40% for TA3. A fairly good agreement between experimental and calculated volume fractions is reached only for the Ni-rich composition (TA4). The same trend is observed regarding transition temperatures. As predicted by the TCHEA3 database, experimental results confirm the presence of an FCC single-phase domain between solvus

and solidus temperatures for all alloys. The solidus temperature is well-described for the Ni-rich TA4 but significative differences are evidenced for other compositions for which the temperature is systematically underestimated (52°C for TA1 to 78°C for TA5). In contrast, the solvus temperature looks well described in the TCHEA3 database for TA1, TA2, TA3 and TA5 (Table 1) but is under evaluated for TA4 (52°C lower than experimentally assessed). The latter trend is in line with a recent work on quinary (Ni,Co)-based superalloys by Llewelyn *et al.* [61]. In their study of elemental partitioning in the Al–Co–Ni–Ti system, authors have pointed out consistency between experimental and calculated solvus temperatures using TCNI8 database for high Co content but significant differences at lower Co content.

The results also emphasize several discrepancies between predicted phases and experimentally observed ones. In particular, the Al- and Cr-free quaternary TA6 alloy was predicted to be $L1_2$ single-phase material at 1000°C (Fig. S5). Calculations suggest that the extent of the $L1_2$ region in the database is large T >~ 820°C (1093K) and in a broad range of Fe addition (Fig. S6). However, a multi-phased microstructure is evidenced and three phases were unambiguously identified (FCC, $L1_2$, τ) (Fig. 7). The presence of the $(Ni_{0.5}Co_{0.5})_3Ti$ (τ) ternary phase of hexagonal structure with the Co_3V prototype is commonly observed in Co–Ni–Ti alloying systems and has been first identified by Van Loo and Bastin in the ternary system at 900°C using diffusion couple technique [62]. It has been evidenced as a stable phase between 800°C and 1100°C in recent studies [63–67]. The ternary phase is present in a narrow compositional region of the Co–Ni–Ti system between Ni_3Ti ($D0_{24}$) and Co_3Ti ($L1_2$) for [Ti] ~ 25 at.%, 25 at.% < [Ni] < 55 at.%, 20 at.% < [Co] < 50 at.%, between 800°C and 1100°C. Riani *et al.* suggest that Ni_3Ti, τ and Co_3Ti own related structures with different stacking sequence and coordination geometry [65]. The discrepancies between calculated and experimental phase diagrams can be explained by a poor description of the calculated Co–Ni–Ti system. The ternary diagram has not been fully assessed in the TCHEA3 database and the τ phase is not included in the database [56] leading to a wrong prediction of the TA6 microstructure at 1000°C (figure 4c). Finally, it should be mentioned that the extent of this ternary phase may be quite large in the quaternary system as a two-phase FCC+τ domain has been experimentally confirmed for the $Co_{52.5}Ni_{35}Ti_{12.5}$ composition ([Fe] = 0 at.%, Fig. S6) between 800°C and 1100°C [64,66,67]. Calphad predictions suggest two phases for the considered alloy composition: FCC and Ni_3Ti.

4.2. Unexpected features of the predicted FCC+$L1_2$ two-phase region

From the mapping of the calculated alloy compositions exhibiting FCC+$L1_2$ microstructure at both 800°C and 1000°C (Fig. 4), it has been reported that Cr and Fe additions leads to a strong decrease of the number of potential compositions with a duplex microstructure. Cr and Fe promote the formation of undesirable phases (B2, σ, Laves, mainly). However, a clear increase of the $L1_2$ phase fraction is

observed with increasing Cr nominal content in the alloy compositions exhibiting FCC+$L1_2$ microstructure (Fig. 4c). The effect may be explained by the elemental partitioning between FCC and $L1_2$ phases. The analysis of the current high throughput calculations (§3.1.1) indicates that Cr preferentially partitions to the FCC phase (Fig. S1a). The alloy enrichment in Cr decreases Al and Ti solubilities in both FCC and $L1_2$ phases (Fig. S4a,b), thus inducing an increase of the $L1_2$ volume fraction. On the contrary, an alloy enrichment in Fe has no pronounced effect on the $L1_2$ phase fraction (Fig. 4c). Fe partitions mainly toward the FCC phase but the increase of the Fe nominal content does not significantly reduce the solubility of Al and Ti in the FCC phase (Fig. S4c). However, calculations indicate that Fe addition enhances the $L1_2$ phase fraction in a restricted (Ni,Al)-rich regions up to a threshold ([Fe] = 20 at.%) after which the FCC+$L1_2$ region disappears (Fig. 4c and S5). It could be explained considering the existence of the Ni_3Fe phase with $L1_2$ structure [68], stable for T < 600°C in the Ni–Fe phase diagram. In the ternary Al–Fe–Ni system [69,70], the $L1_2$ phase originating from the binary Al–Ni system progressively extends towards Ni_3Fe until a complete solubility is observed at temperatures below 600°C (Fig. S7). This explains the increase of the $L1_2$ content at 800°C in the Fe-rich alloys in the senary system.

4.3. On the alloying strategy to design FCC+$L1_2$ complex concentrated alloys

The results of the calculations in the Al–Co–Cr–Ni–Fe–Ti system clearly point out the prominent role of the (Ni,Co) group on the stability of the FCC+$L1_2$ domain. Therefore, Co appears as the main substitute of Ni to get a stable FCC+$L1_2$ microstructure at elevated temperatures. The phase diagram sections for [Cr] = [Fe] = 0 at.% and [Cr] = [Fe] = 10 at.% (Fig. 4c) are given in figure 8 with a focus on the equilibrium phases. The superposition allows to better visualize the way in which the FCC+$L1_2$ domain is reduced by Cr and Fe additions (Fig. 8c). A limited number of FCC+$L1_2$ compositions is expected in the (Co,Al)-rich region for [Fe] = [Cr] = 10 at.% due to the growing presence of the B2 phase (Fig. 8b, bottom right-corner). A similar tendency is observed in the (Co,Ti)-rich region (Fig. 8b, bottom left-corner) due to the emergence of Laves phases. The destabilizing effect of alloying on FCC+$L1_2$ microstructures based on (Co,Ti) has already been established as the main issue for the development of such alloys for high temperature applications [71,72].

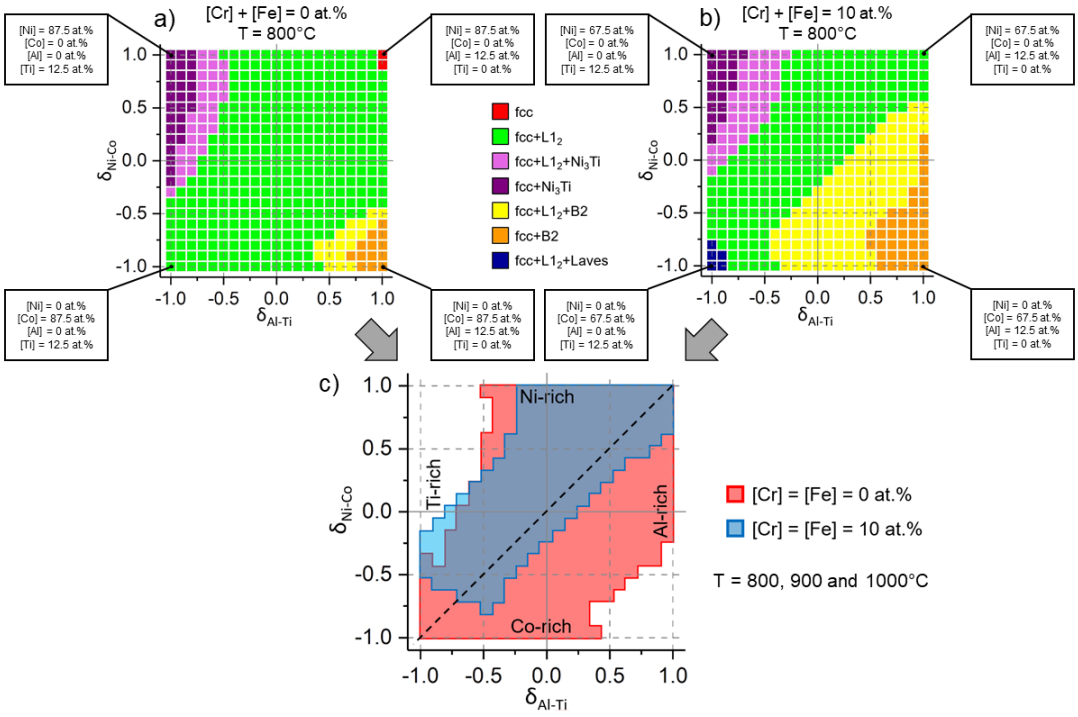

Figure 8: Phase diagram section at 800°C for [Al] + [Ti] = 12.5 at.% and a) [Cr] = [Fe] = 0 at.%; b) [Cr] = [Fe] = 10 at.%. c) Overlap of the FCC+L1$_2$ phase regions at 800°C, 900°C and 1000°C for [Cr] = [Fe] = 0 at.% (red) and [Cr] = [Fe] = 10 at.% (blue). The average differences between Ni and Co ($\delta_{Ni-Co} = \frac{[Ni]-[Co]}{[Ni]+[Co]}$) and between Al and Ti ($\delta_{Al-Ti} = \frac{[Al]-[Ti]}{[Al]+[Ti]}$) were considered as axes in order to overlap the FCC+L1$_2$ regions shown in a) and b).

With increasing Cr and Fe content, the substitution path from (Ni,Al)-based alloys to (Co,Ti)-ones narrows (Fig. 8c). In that respect, Co–Ni substitutions must be carefully tailored with Ti–Al substitutions. Therefore, quinary alloys in Al–Co–Cr–Fe–Ni and Co–Cr–Fe–Ni–Ti systems designed with high Cr and Fe contents and [Ni] = [Co] will lead to the precipitation of B2 and Ni_3Ti phases, respectively [45,73,74].

The plot of Al–Co–Ni–Ti phase diagrams sections at constant Cr and Fe content makes accessible the design of FCC+L1$_2$ alloys. As potential alloy compositions with FCC+L1$_2$ microstructures are mainly expanded along the (Ni,Al) – (Co,Ti) axis (dashed line in Fig. 8c), possible Co–Ni substitutions may be selected by carefully tailoring the $\frac{[Ti]}{[Al]}$ ratio. Additionally, the current alloying design requires the following methodology. The [Al] + [Ti] content is first selected. By sweeping with [Cr] and [Fe] content for the defined [Al] + [Ti], the phase diagram sections will give the available Al–Ti and Co–Ni proportions and then limit the compositional space to get the desired (predicted) microstructure. Moreover, such a representation at different temperatures may be a convenient way to avoid undesirable phases and secure a large solution treatment window.

The current study highlights that the [Al] + [Ti] content could be tailored to meet the desired $L1_2$ phase fraction. However, the fraction of ordered phase could significantly differ and depends on the region of the Al–Co–Ni–Ti quaternary section (Fig. 4c). Once a nominal alloy composition is chosen, the amount of $L1_2$ phase can be optimized using a combination of lever rule calculation and isopleth plot from the FCC composition to the $L1_2$ one at a given temperature. The isopleth allows to make sure that no other phases appears at lower or higher temperatures. This way, the nominal composition is adapted to keep the same FCC and $L1_2$ compositions but with different $L1_2$ fraction.

As previously established, Ni and Co are key elements in FCC+$L1_2$ compositions but their different partitioning behaviors raise some issues regarding the design of $L1_2$-strengthened HEAs/CCAs based exclusively on nominal alloy compositions. Indeed, the selection of candidates with equimolar nominal contents in Co, Cr, Fe and Ni will mainly lead to the formation of Co-rich FCC solid solutions and low volume fractions of Ni-rich $L1_2$ precipitates. First reported $L1_2$-strengthened-HEAs/CCAs have usually been designed this way [24,32,37,39,43,49,50]. The prepared alloys usually do not exceed 20% of $L1_2$ phase fraction at 800°C whereas optimal $L1_2$ volume fraction is achieved around 65-70% in single-crystal Ni-based superalloys [75]. The design of HEAs/CCAs with higher $L1_2$ volume fractions is thus challenging and requires to tailor the nominal alloy composition to the partitioning behavior of each alloying element. Since Ni partitions mainly to the FCC phase, the increase of the $L1_2$ phase fraction will require a significant increase of the Ni nominal content. Hence, a 70% $L1_2$ phase fraction would be achieved for [Ni] = 50 at.% in CCAs, which is the usual content in Ni-based superalloys. Moreover, highly substituted FCC solid solutions and $L1_2$ phase would be achieved for very different nominal compositions. For instance, $L1_2$ phase with [Ni] = [Co], [Al] = [Ti], and FCC solid solution with [Ni] = [Co] = [Cr] = [Fe] would be reached at 800°C for [Al] + [Ti] = 12.5 at.% with nominal $Al_{6.2}Co_{47.1}Cr_{13.1}Fe_{3.1}$ $Ni_{24.2}Ti_{6.3}$ (at.%) and $Al_5Co_{18.3}Cr_{13.4}Fe_{14.5}$ $Ni_{41.3}Ti_{7.5}$ (at.%) alloy compositions, respectively. Most of FCC+$L1_2$ compositions with a higher $L1_2$ volume fraction have been designed with a high Ni content, leading to a **concentrated** FCC phase [30,31,35,40].

Therefore, it should be mentioned that Fe has a significant contribution as a substitute of the (Ni,Co) group in the FCC phase and could enhance solid solution strengthening. Fe appears also as the only element able to provide some adequate degree of substitution to deviate from Ni-based superalloys compositions [38]. Such use of Fe as substitute element has been recently reported with the purpose to design precipitation hardened Co-free HEAs [38]. It is however challenging to get the duplex FCC+$L1_2$ microstructure as a large amount of Fe is required and is not compatible with a high Cr content [38]. A significant number of Al–Co–Cr–Ni–Ti quinary alloys have also been investigated within the framework of (Ni,Co)-based superalloys [61,76]. It seems that extending from Ni-based compositions to (Ni,Co)-based ones can positively impact HT properties [77]. However, the current study highlights that a substantial amount of Fe can be added to achieve compositions leading to

(Ni,Co,Fe)-based superalloys. Future studies should be devoted to the way Fe may affect the matrix and the precipitates for different (Ni,Co) contents and could finally impact HT properties.

5. Conclusions

The extent of the FCC+$L1_2$ two-phase region in the Al–Co–Cr–Fe–Ni–Ti system has been investigated at HT (800-1000°C) using the Calphad approach and the TCHEA3 database. On the basis of the calculations, six alloys were designed, processed and characterized to assess the reliability of the thermodynamic predictions. The following results were obtained:

1. the FCC+$L1_2$ two-phase region is sparsely extended in the senary system at 800°C and 1000°C. Only 4 562 alloy compositions on the 79 695 analyzed ones were predicted to have a duplex microstructure at both temperatures.
2. the Al–Co–Ni–Ti quaternary system is found to be the key component giving rise to the FCC+$L1_2$ two-phase region in the highest order system. Additions of Fe and Cr reduce significantly the size of the two-phase domain and tend to stabilize the formation of B2 and Ni_3Ti/Laves phases in (Co-Al)-rich and (Ni-Ti)-rich alloy compositions, respectively. Addition of Cr exceeding 25 at.% does not allow to reach the desired microstructure in the calculated temperature range.
3. with a large solubility of Fe in the FCC phase, Fe appears as an interesting substitution element for Co or Ni in multicomponent systems. Studies on some new (Ni,Co,Fe)-based compositions are suggested for future development of $L1_2$-strengthened HEAs/CCAs.
4. first experimental results on the predicted FCC+$L1_2$ compositions indicates that the TCHEA3 database appear reliable to describe peculiarities of the FCC and $L1_2$ two-phase region. However, equilibrium phases in Al- and Cr-free alloys of the Co–Fe–Ni–Ti system are incorrectly described due to the absence of the ternary τ $(Ni_{0.5}Co_{0.5})_3Ti$ phase in the database.
5. a new visualization method of the FCC+$L1_2$ region in the senary Al–Co–Cr–Fe–Ni–Ti is proposed. The method relies on the representation of phase diagrams sections from the Al–Co–Ni–Ti quaternary system considering elemental substitutions in three distinct groups, (Ni,Co), (Cr,Fe) and (Al,Ti). We believe that the methodology used in this paper will be helpful to design new $L1_2$-strengthened HEAs/CCAs.

Acknowledgments

The authors would like to acknowledge the French National Research Agency (ANR) for the support through the ANR 16-CE08-0027 “TURBO-AHEAD” program. The technical support of Julie Bourgon, Yvan Cotrebil and Rémy Pirès was greatly appreciated.

References

[1] B. Cantor, I.T.H. Chang, P. Knight, A.J.B. Vincent, Microstructural development in equiatomic multicomponent alloys, Mater. Sci. Eng. A. 375–377 (2004) 213–218. https://doi.org/10.1016/j.msea.2003.10.257.

[2] J.-W. Yeh, S.-K. Chen, S.-J. Lin, J.-Y. Gan, T.-S. Chin, T.-T. Shun, C.-H. Tsau, S.-Y. Chang, Nanostructured High-Entropy Alloys with Multiple Principal Elements: Novel Alloy Design Concepts and Outcomes, Adv. Eng. Mater. 6 (2004) 299–303. https://doi.org/10.1002/adem.200300567.

[3] S. Gorsse, J.-P. Couzinie, D.B. Miracle, From high-entropy alloys to complex concentrated alloys, Comptes Rendus Phys. 19 (2018) 721–736. https://doi.org/10.1016/j.crhy.2018.09.004.

[4] D.B. Miracle, O.N. Senkov, A critical review of high entropy alloys and related concepts, Acta Mater. 122 (2017) 448–511. https://doi.org/10.1016/j.actamat.2016.08.081.

[5] Z. Li, S. Zhao, R.O. Ritchie, M.A. Meyers, Mechanical properties of high-entropy alloys with emphasis on face-centered cubic alloys, Prog. Mater. Sci. 102 (2019) 296–345. https://doi.org/10.1016/j.pmatsci.2018.12.003.

[6] O.N. Senkov, G.B. Wilks, D.B. Miracle, C.P. Chuang, P.K. Liaw, Refractory high-entropy alloys, Intermetallics. 18 (2010) 1758–1765. https://doi.org/10.1016/j.intermet.2010.05.014.

[7] O.N. Senkov, D.B. Miracle, K.J. Chaput, J.-P. Couzinie, Development and Exploration of Refractory High Entropy Alloys – A Review, J. Mater. Res. 33 (2018) 3092–3128. https://doi.org/10.1557/jmr.2018.153.

[8] J.-P. Couzinie, G. Dirras, Body-centered cubic high-entropy alloys: From processing to underlying deformation mechanisms, Mater. Charact. 147 (2019) 533–544. https://doi.org/10.1016/j.matchar.2018.07.015.

[9] S. Gorsse, D.B. Miracle, O.N. Senkov, Mapping the world of complex concentrated alloys, Acta Mater. 135 (2017) 177–187. https://doi.org/10.1016/j.actamat.2017.06.027.

[10] F. Otto, A. Dlouhy, C. Somsen, H. Bei, G. Eggeler, E.P. George, The influences of temperature and microstructure on the tensile properties of a CoCrFeMnNi high-entropy alloy, Acta Mater. 61 (2013) 5743–5755. https://doi.org/10.1016/j.actamat.2013.06.018.

[11] F. Otto, N.L. Hanold, E.P. George, Microstructural evolution after thermomechanical processing in an equiatomic, single-phase CoCrFeMnNi high-entropy alloy with special focus on twin boundaries, Intermetallics. 54 (2014) 39–48. https://doi.org/10.1016/j.intermet.2014.05.014.

[12] G. Laplanche, O. Horst, F. Otto, G. Eggeler, E.P. George, Microstructural evolution of a CoCrFeMnNi high-entropy alloy after swaging and annealing, J. Alloys Compd. 647 (2015) 548–557. https://doi.org/10.1016/j.jallcom.2015.05.129.

[13] G. Laplanche, P. Gadaud, O. Horst, F. Otto, G. Eggeler, E.P. George, Temperature dependencies of the elastic moduli and thermal expansion coefficient of an equiatomic, single-phase CoCrFeMnNi high-entropy alloy, J. Alloys Compd. 623 (2015) 348–353. https://doi.org/10.1016/j.jallcom.2014.11.061.

[14] G. Laplanche, A. Kostka, O.M. Horst, G. Eggeler, E.P. George, Microstructure evolution and critical stress for twinning in the CrMnFeCoNi high-entropy alloy, Acta Mater. 118 (2016) 152–163. https://doi.org/10.1016/j.actamat.2016.07.038.

[15] G. Bracq, M. Laurent-Brocq, C. Varvenne, L. Perrière, W.A. Curtin, J.-M. Joubert, I. Guillot, Combining experiments and modeling to explore the solid solution strengthening of high and

medium entropy alloys, Acta Mater. 177 (2019) 266–279. https://doi.org/10.1016/j.actamat.2019.06.050.
[16] M. Laurent-Brocq, A. Akhatova, L. Perrière, S. Chebini, X. Sauvage, E. Leroy, Y. Champion, Insights into the phase diagram of the CrMnFeCoNi high entropy alloy, Acta Mater. 88 (2015) 355–365. https://doi.org/10.1016/j.actamat.2015.01.068.
[17] G. Bracq, M. Laurent-Brocq, L. Perrière, R. Pirès, J.-M. Joubert, I. Guillot, The fcc solid solution stability in the Co-Cr-Fe-Mn-Ni multi-component system, Acta Mater. 128 (2017) 327–336. https://doi.org/10.1016/j.actamat.2017.02.017.
[18] B. Gludovatz, A. Hohenwarter, D. Catoor, E.H. Chang, E.P. George, R.O. Ritchie, A fracture-resistant high-entropy alloy for cryogenic applications, Science. 345 (2014) 1153–1158. https://doi.org/10.1126/science.1254581.
[19] Z. Zhang, M.M. Mao, J. Wang, B. Gludovatz, Z. Zhang, S.X. Mao, E.P. George, Q. Yu, R.O. Ritchie, Nanoscale origins of the damage tolerance of the high-entropy alloy CrMnFeCoNi, Nat. Commun. 6 (2015) 10143. https://doi.org/10.1038/ncomms10143.
[20] S. Huang, W. Li, S. Lu, F. Tian, J. Shen, E. Holmström, L. Vitos, Temperature dependent stacking fault energy of FeCrCoNiMn high entropy alloy, Scr. Mater. 108 (2015) 44–47. https://doi.org/10.1016/j.scriptamat.2015.05.041.
[21] Y.H. Zhang, Y. Zhuang, A. Hu, J.J. Kai, C.T. Liu, The origin of negative stacking fault energies and nano-twin formation in face-centered cubic high entropy alloys, Scr. Mater. 130 (2017) 96–99. https://doi.org/10.1016/j.scriptamat.2016.11.014.
[22] S. Gialanella, A. Malandruccolo, Aerospace Alloys, Springer Nature, 2019.
[23] D.B. Miracle, O.N. Senkov, A critical review of high entropy alloys and related concepts, Acta Mater. 122 (2017) 448–511. https://doi.org/10.1016/j.actamat.2016.08.081.
[24] W.H. Liu, T. Yang, C.T. Liu, Precipitation hardening in CoCrFeNi-based high entropy alloys, Mater. Chem. Phys. 210 (2018) 2–11. https://doi.org/10.1016/j.matchemphys.2017.07.037.
[25] S. Dasari, A. Jagetia, Y.-J. Chang, V. Soni, B. Gwalani, S. Gorsse, A.-C. Yeh, R. Banerjee, Engineering multi-scale B2 precipitation in a heterogeneous FCC based microstructure to enhance the mechanical properties of a Al0.5Co1.5CrFeNi1.5 high entropy alloy, J. Alloys Compd. (2020) 154707. https://doi.org/10.1016/j.jallcom.2020.154707.
[26] J.Y. He, H. Wang, H.L. Huang, X.D. Xu, M.W. Chen, Y. Wu, X.J. Liu, T.G. Nieh, K. An, Z.P. Lu, A precipitation-hardened high-entropy alloy with outstanding tensile properties, Acta Mater. 102 (2016) 187–196. https://doi.org/10.1016/j.actamat.2015.08.076.
[27] J.Y. He, H. Wang, Y. Wu, X.J. Liu, H.H. Mao, T.G. Nieh, Z.P. Lu, Precipitation behavior and its effects on tensile properties of FeCoNiCr high-entropy alloys, Intermetallics. 79 (2016) 41–52. https://doi.org/10.1016/j.intermet.2016.09.005.
[28] H. Peng, L. Hu, L. Li, J. Gao, Q. Zhang, On the correlation between L12 nanoparticles and mechanical properties of (NiCo)52+2x(AlTi)4+2xFe29-4xCr15 (x=0-4) high-entropy alloys, J. Alloys Compd. 817 (2020) 152750. https://doi.org/10.1016/j.jallcom.2019.152750.
[29] K. Ming, X. Bi, J. Wang, Realizing strength-ductility combination of coarse-grained Al 0.2 Co 1.5 CrFeNi 1.5 Ti 0.3 alloy via nano-sized, coherent precipitates, Int. J. Plast. 100 (2018) 177–191. https://doi.org/10.1016/j.ijplas.2017.10.005.
[30] Z.G. Wang, W. Zhou, L.M. Fu, J.F. Wang, R.C. Luo, X.C. Han, B. Chen, X.D. Wang, Effect of coherent L1 2 nanoprecipitates on the tensile behavior of a fcc-based high-entropy alloy, Mater. Sci. Eng. A. 696 (2017) 503–510. https://doi.org/10.1016/j.msea.2017.04.111.
[31] H.M. Daoud, A.M. Manzoni, N. Wanderka, U. Glatzel, High-Temperature Tensile Strength of Al10Co25Cr8Fe15Ni36Ti6 Compositionally Complex Alloy (High-Entropy Alloy), JOM. 67 (2015) 2271–2277. https://doi.org/10.1007/s11837-015-1484-7.
[32] Y.L. Zhao, T. Yang, Y. Tong, J. Wang, J.H. Luan, Z.B. Jiao, D. Chen, Y. Yang, A. Hu, C.T. Liu, J.-J. Kai, Heterogeneous precipitation behavior and stacking-fault-mediated deformation in a CoCrNi-based medium-entropy alloy, Acta Mater. 138 (2017) 72–82. https://doi.org/10.1016/j.actamat.2017.07.029.
[33] Y.-J. Chang, A.-C. Yeh, The evolution of microstructures and high temperature properties of AlxCo1.5CrFeNi1.5Tiy high entropy alloys, J. Alloys Compd. 653 (2015) 379–385. https://doi.org/10.1016/j.jallcom.2015.09.042.

[34] S. Antonov, M. Detrois, S. Tin, Design of Novel Precipitate-Strengthened Al-Co-Cr-Fe-Nb-Ni High-Entropy Superalloys, Metall. Mater. Trans. A. 49 (2018) 305–320. https://doi.org/10.1007/s11661-017-4399-9.
[35] T.-K. Tsao, A.-C. Yeh, C.-M. Kuo, K. Kakehi, H. Murakami, J.-W. Yeh, S.-R. Jian, The High Temperature Tensile and Creep Behaviors of High Entropy Superalloy, Sci. Rep. 7 (2017). https://doi.org/10.1038/s41598-017-13026-7.
[36] Y.Y. Zhao, H.W. Chen, Z.P. Lu, T.G. Nieh, Thermal stability and coarsening of coherent particles in a precipitation-hardened (NiCoFeCr) 94 Ti 2 Al 4 high-entropy alloy, Acta Mater. 147 (2018) 184–194. https://doi.org/10.1016/j.actamat.2018.01.049.
[37] B. Han, J. Wei, Y. Tong, D. Chen, Y. Zhao, J. Wang, F. He, T. Yang, C. Zhao, Y. Shimizu, K. Inoue, Y. Nagai, A. Hu, C.T. Liu, J.J. Kai, Composition evolution of gamma prime nanoparticles in the Ti-doped CoFeCrNi high entropy alloy, Scr. Mater. 148 (2018) 42–46. https://doi.org/10.1016/j.scriptamat.2018.01.025.
[38] Y.L. Zhao, T. Yang, J.H. Zhu, D. Chen, Y. Yang, A. Hu, C.T. Liu, J.-J. Kai, Development of high-strength Co-free high-entropy alloys hardened by nanosized precipitates, Scr. Mater. 148 (2018) 51–55. https://doi.org/10.1016/j.scriptamat.2018.01.028.
[39] B. Gwalani, V. Soni, D. Choudhuri, M. Lee, J.Y. Hwang, S.J. Nam, H. Ryu, S.H. Hong, R. Banerjee, Stability of ordered L1 2 and B 2 precipitates in face centered cubic based high entropy alloys - Al 0.3 CoFeCrNi and Al 0.3 CuFeCrNi 2, Scr. Mater. 123 (2016) 130–134. https://doi.org/10.1016/j.scriptamat.2016.06.019.
[40] A. Yeh, T. Tsao, Y. Chang, K. Chang, J. Yeh, M. Chiou, S. Jian, C. Kuo, W. Wang, H. Murakami, Developing New Type of High Temperature Alloys – High Entropy Superalloys, Int. J. Metall. Mater. Eng. 1 (2015). https://doi.org/10.15344/2455-2372/2015/107.
[41] L. Zhang, Y. Zhou, X. Jin, X. Du, B. Li, The microstructure and high-temperature properties of novel nano precipitation-hardened face centered cubic high-entropy superalloys, Scr. Mater. 146 (2018) 226–230. https://doi.org/10.1016/j.scriptamat.2017.12.001.
[42] A. Manzoni, S. Singh, H. Daoud, R. Popp, R. Völkl, U. Glatzel, N. Wanderka, On the Path to Optimizing the Al-Co-Cr-Cu-Fe-Ni-Ti High Entropy Alloy Family for High Temperature Applications, Entropy. 18 (2016) 104. https://doi.org/10.3390/e18040104.
[43] T. Yang, Y.L. Zhao, Y. Tong, Z.B. Jiao, J. Wei, J.X. Cai, X.D. Han, D. Chen, A. Hu, J.J. Kai, K. Lu, Y. Liu, C.T. Liu, Multicomponent intermetallic nanoparticles and superb mechanical behaviors of complex alloys, Science. 362 (2018) 933–937. https://doi.org/10.1126/science.aas8815.
[44] Y.L. Zhao, T. Yang, Y.R. Li, L. Fan, B. Han, Z.B. Jiao, D. Chen, C.T. Liu, J.J. Kai, Superior high-temperature properties and deformation-induced planar faults in a novel L12-strengthened high-entropy alloy, Acta Mater. 188 (2020) 517–527. https://doi.org/10.1016/j.actamat.2020.02.028.
[45] D. Chen, F. He, B. Han, Q. Wu, Y. Tong, Y. Zhao, Z. Wang, J. Wang, J. Kai, Synergistic effect of Ti and Al on L12-phase design in CoCrFeNi-based high entropy alloys, Intermetallics. 110 (2019) 106476. https://doi.org/10.1016/j.intermet.2019.106476.
[46] T. Yang, Y. Zhao, W. Liu, J. Kai, C. Liu, L12-strengthened high-entropy alloys for advanced structural applications, J. Mater. Res. 33 (2018) 2983–2997. https://doi.org/10.1557/jmr.2018.186.
[47] B. Gwalani, S. Gorsse, V. Soni, M. Carl, N. Ley, J. Smith, A.V. Ayyagari, Y. Zheng, M. Young, R.S. Mishra, R. Banerjee, Role of copper on L12 precipitation strengthened fcc based high entropy alloy, Materialia. 6 (2019) 100282. https://doi.org/10.1016/j.mtla.2019.100282.
[48] H.M. Daoud, A. Manzoni, R. Voelkl, N. Wanderka, U. Glatzel, Microstructure and Tensile Behavior of Al8Co17Cr17Cu8Fe17Ni33 (at.%) High-Entropy Alloy, Jom. 65 (2013) 1805–1814. https://doi.org/10.1007/s11837-013-0756-3.
[49] J.Y. He, H. Wang, Y. Wu, X.J. Liu, H.H. Mao, T.G. Nieh, Z.P. Lu, Precipitation behavior and its effects on tensile properties of FeCoNiCr high-entropy alloys, Intermetallics. 79 (2016) 41–52. https://doi.org/10.1016/j.intermet.2016.09.005.
[50] J.Y. He, H. Wang, H.L. Huang, X.D. Xu, M.W. Chen, Y. Wu, X.J. Liu, T.G. Nieh, K. An, Z.P. Lu, A precipitation-hardened high-entropy alloy with outstanding tensile properties, Acta Mater. 102 (2016) 187–196. https://doi.org/10.1016/j.actamat.2015.08.076.

[51] T. Yang, Y.L. Zhao, J.H. Luan, B. Han, J. Wei, J.J. Kai, C.T. Liu, Nanoparticles-strengthened high-entropy alloys for cryogenic applications showing an exceptional strength-ductility synergy, Scr. Mater. 164 (2019) 30–35. https://doi.org/10.1016/j.scriptamat.2019.01.034.
[52] O.N. Senkov, J.D. Miller, D.B. Miracle, C. Woodward, Accelerated exploration of multi-principal element alloys with solid solution phases, Nat. Commun. 6 (2015). https://doi.org/10.1038/ncomms7529.
[53] F. Tancret, I. Toda-Caraballo, E. Menou, P.E.J. Rivera Díaz-Del-Castillo, Designing high entropy alloys employing thermodynamics and Gaussian process statistical analysis, Mater. Des. 115 (2017) 486–497. https://doi.org/10.1016/j.matdes.2016.11.049.
[54] J.M. Rickman, H.M. Chan, M.P. Harmer, J.A. Smeltzer, C.J. Marvel, A. Roy, G. Balasubramanian, Materials informatics for the screening of multi-principal elements and high-entropy alloys, Nat. Commun. 10 (2019). https://doi.org/10.1038/s41467-019-10533-1.
[55] A. Abu-Odeh, E. Galvan, T. Kirk, H. Mao, Q. Chen, P. Mason, R. Malak, R. Arróyave, Efficient exploration of the High Entropy Alloy composition-phase space, Acta Mater. 152 (2018) 41–57. https://doi.org/10.1016/j.actamat.2018.04.012.
[56] TCHEA3: TCS High Entropy Alloy Database, (n.d.). https://www.thermocalc.com/media/35873/tchea3_extended_info.pdf (accessed July 9, 2019).
[57] C.Y. Cui, Y.F. Gu, D.H. Ping, H. Harada, Phase constituents in Ni–Al–Co–Ti quaternary alloys, Intermetallics. 16 (2008) 910–916. https://doi.org/10.1016/j.intermet.2008.04.006.
[58] J. Rodriguez-Carvajal, FULLPROF: A Program for Rietveld Refinement and Pattern Matching Analysis, Abstr. Satell. Meet. Powder Diffr. XV Congr. IUCr. Toulouse, France (1990) 127.
[59] D.L. Sponseller, Differential thermal analysis of nickel-base superalloys, Superalloys. (1996) 259–270.
[60] J.P. Minshull, S. Neumeier, M.G. Tucker, H.J. Stone, A1-$L1_2$ Structures in the Al-Co-Ni-Ti Quaternary Phase System, Adv. Mater. Res. 278 (2011) 399–404. https://doi.org/10.4028/www.scientific.net/AMR.278.399.
[61] S.C.H. Llewelyn, K.A. Christofidou, V.J. Araullo-Peters, N.G. Jones, M.C. Hardy, E.A. Marquis, H.J. Stone, The effect of Ni:Co ratio on the elemental phase partitioning in γ-γ′ Ni-Co-Al-Ti-Cr alloys, Acta Mater. 131 (2017) 296–304. https://doi.org/10.1016/j.actamat.2017.03.067.
[62] F.J.J. Van Loo, G.F. Bastin, Phase relations and diffusion paths in the Ti-Ni-Co system at 900° C, J. Common Met. 81 (1981) 61–69.
[63] C. Zhou, C. Guo, J. Li, C. Li, Z. Du, Experimental investigations of the Co–Ni–Ti system: Liquidus surface projection and isothermal section at 1373 K, J. Alloys Compd. 754 (2018) 268–282. https://doi.org/10.1016/j.jallcom.2018.04.253.
[64] C. Zhou, C. Guo, C. Li, Z. Du, Experimental determination and thermodynamic assessment of the Co–Ni–Ti system, Calphad. 63 (2018) 61–76. https://doi.org/10.1016/j.calphad.2018.08.011.
[65] P. Riani, K. Sufryd, G. Cacciamani, Critical assessment and experimental investigation of Co–Ni–Ti phase equilibria, Calphad. 44 (2014) 26–38. https://doi.org/10.1016/j.calphad.2013.06.008.
[66] Y. Yuan, L. Yang, D. Li, A. Tang, F. Pan, H. Seifert, N. Moelans, Diffusion multiple study of Co-Ni-Ti system at 1073 K, Calphad. 63 (2018) 156–163. https://doi.org/10.1016/j.calphad.2018.09.007.
[67] H. Li, P. Zhou, Y. Du, Z. Jin, Isothermal sections of the Co-Ni-Ti system at 950 and 1000°C, Int. J. Mater. Res. 109 (2018) 105–112. https://doi.org/10.3139/146.111587.
[68] G. Cacciamani, J. De Keyzer, R. Ferro, U.E. Klotz, J. Lacaze, P. Wollants, Critical evaluation of the Fe–Ni, Fe–Ti and Fe–Ni–Ti alloy systems, Intermetallics. 14 (2006) 1312–1325. https://doi.org/10.1016/j.intermet.2005.11.028.
[69] S. Ochial, Y. Oya, T. Suzuki, Alloying behaviour of Ni3Al, Ni3Ga, Ni3Si and Ni3Ge, Acta Metall. 32 (1984) 289–298. https://doi.org/10.1016/0001-6160(84)90057-9.
[70] Y. Himuro, Y. Tanaka, N. Kamiya, I. Ohnuma, R. Kainuma, K. Ishida, Stability of ordered L12 phase in Ni3Fe–Ni3X (X:Si and Al) pseudobinary alloys, Intermetallics. 12 (2004) 635–643. https://doi.org/10.1016/j.intermet.2004.03.008.
[71] J.M. Blaise, P. Viatour, J.M. Drapier, On the stability and precipitation of the Co3Ti phase in Co-Ti alloys, Cobalt. (1970).
[72] P. Viatour, J.M. Drapier, D. Coutsouradis, Stability of the gamma prime Co3Ti compound in simple and complex Co alloys, Cobalt. (1973).

[73] F. He, Z. Wang, B. Han, Q. Wu, D. Chen, J. Li, J. Wang, C.T. Liu, J.J. Kai, Solid solubility, precipitates, and stacking fault energy of micro-alloyed CoCrFeNi high entropy alloys, J. Alloys Compd. 769 (2018) 490–502. https://doi.org/10.1016/j.jallcom.2018.07.336.
[74] A.-C. Yeh, Y.-J. Chang, C.-W. Tsai, Y.-C. Wang, J.-W. Yeh, C.-M. Kuo, On the Solidification and Phase Stability of a Co-Cr-Fe-Ni-Ti High-Entropy Alloy, Metall. Mater. Trans. A. 45 (2014) 184–190. https://doi.org/10.1007/s11661-013-2097-9.
[75] T. Murakumo, T. Kobayashi, Y. Koizumi, H. Harada, Creep behaviour of Ni-base single-crystal superalloys with various γ′ volume fraction, Acta Mater. 52 (2004) 3737–3744. https://doi.org/10.1016/j.actamat.2004.04.028.
[76] K.A. Christofidou, N.G. Jones, E.J. Pickering, R. Flacau, M.C. Hardy, H.J. Stone, The microstructure and hardness of Ni-Co-Al-Ti-Cr quinary alloys, J. Alloys Compd. 688 (2016) 542–552. https://doi.org/10.1016/j.jallcom.2016.07.159.
[77] C.H. Zenk, S. Neumeier, N.M. Engl, S.G. Fries, O. Dolotko, M. Weiser, S. Virtanen, M. Göken, Intermediate Co/Ni-base model superalloys — Thermophysical properties, creep and oxidation, Scr. Mater. 112 (2016) 83–86. https://doi.org/10.1016/j.scriptamat.2015.09.018.

Supplementary Materials

Study of the FCC+L12 two-phase region in complex concentrated alloys based on the Al–Co–Cr–Fe–Ni–Ti system

Rieger T., Joubert J.-M., Laurent-Brocq M., Perrière L., Guillot I. and Couzinié J.-P.*
Université Paris Est Creteil, CNRS, ICMPE, UMR7182, F-94320, Thiais, France
* corresponding author. *E-mail address*: couzinie@icmpe.cnrs.fr

1. Elemental partitioning

The elemental partitioning in the FCC+$L1_2$ alloy compositions was determined with the calculation of the partitioning coefficients at 800°C. For a given nominal composition, the coefficient k_A of an element A is defined as the ratio of the concentration of A in the $L1_2$ phase ($[A]_{L1_2}$) to the concentration of A in the FCC phase ($[A]_{fcc}$):

$$k_A = \frac{[A]_{L1_2}}{[A]_{fcc}} \qquad (1)$$

For $k_A > 1$, A is mostly found in the $L1_2$; for $k_A < 1$ A is A is mostly partitioned to the FCC phase. Results are given in the Figure S1. Al, Ni and Ti partition to the $L1_2$ phase (fig. S1 a). In addition, for equivalent nominal concentrations, k_{Ti} is often superior to k_{Al} due to a higher Al solubility in the FCC phase. On the contrary, Co, Cr and Fe (fig. S1 b) partition preferentially to the FCC phase. Co and Ni partitioning behavior is asymmetrical in most of the compositional range. Regarding Cr (fig. S1 c) and Fe (fig. S1 d), k_{Cr} seems to decrease with increasing nominal content. The tendency is less apparent for Fe.

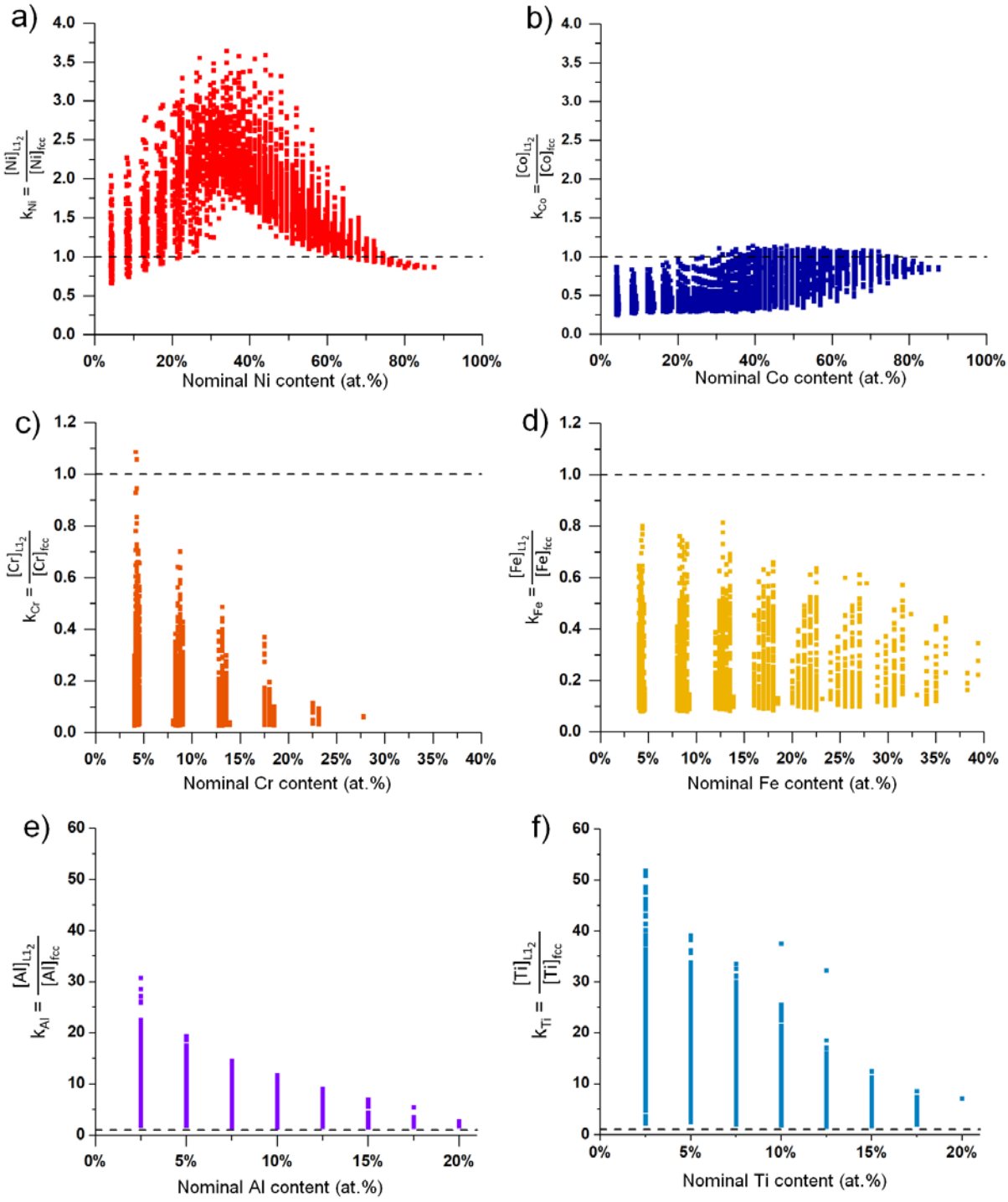

Figure S1: Calculated partitioning coefficients at 800°C for Ni (a), Co (b), Cr (c), Fe (d), Al (e) and Ti (f) as a function of the elemental concentration showing the preferential portioning of Ni, Al and Ti to the $L1_2$ and Co, Cr and Fe to the FCC.

Precise EDX quantitative measurement of the phase concentration is challenging. However, elemental partitioning can be assessed using elemental maps (fig. S2). The preferential partitioning of Co, Cr and Fe to the matrix (FCC) and of Al, Ni and Ti to the precipitates ($L1_2$) is rather obvious in each alloy. The tendency is in good agreement with Calphad predictions.

2. Principal component analysis

The principal component analysis (PCA) is basically a method used to "picture" a dataset from a high dimensional space to a lower one. PCA transforms correlated variables of the given dataset into new ones (factors or eigenvectors) chosen in such a way that the variance is maximized along the relevant directions, using a scalar projection.

In the current study PCA was carried out on the 4 562 (computed) compositions exhibiting an FCC+$L1_2$ duplex microstructure at both 800°C and 1000°C. *The analysis was performed considering compositional variables only (i.e. atomic percentage of the base elements in the selected alloy compositions)*. The eigenvalues of the variance-covariance matrix are given in table S1. The results highlight the existence of a principal component which includes roughly 83% of the total variance (V1). It basically means the dataset is highly spread along this direction in the senary space.

Table S1: Eigenvalues of the variance–covariance matrix for the 4 562 compositions with an FCC+$L1_2$ duplex microstructure at both 800°C and 1000°C.

Variable/ Principal component	Eigenvalue	Ratio	Cumulative ratio
V1	0.0772	83.2%	83.2%
V2	0.0102	11.0%	94.2%
V3	0.0032	3.5%	97.7%
V4	0.0016	1.7%	99.4%
V5	0.0006	0.6%	100.0%

A correlation matrix is then used to link the new principal components to the compositional ones, as defined above (table S2).

Table S2: Correlation matrix between new variables (V1 to V5) and compositional ones.

	V1	V2	V3	V4	V5
Al	0.08	0.15	0.15	0.61	-0.64
Ti	-0.07	-0.08	0.11	-0.76	-0.48
Cr	0.02	0.00	-0.91	0.03	0.08
Fe	0.02	-0.82	0.22	0.17	0.28
Co	-0.73	0.27	0.20	0.06	0.35
Ni	0.67	0.40	0.23	-0.10	0.40
Ratio	83.2%	11.0%	3.5%	1.7%	0.6%

The analysis of the Table S2 gives strong indications of the correlations between chemical elements in the dataset relative to the 4 562 compositions with an FCC+$L1_2$ duplex microstructure at both 800°C and 1000°C. Hence, the V1 principal component is negatively and positively correlated – with fairly close (absolute) values – to Co and Ni, respectively. The result suggests the Co and Ni content in the nominal alloy compositions are preferred directions of the FCC+$L1_2$ two-phase region in the senary space, and justifies the representation of the dataset along an axis such as [Ni] + [Co] is constant *i.e.* the increase of the Ni content may be offset by a decrease of Co (Co and Ni substitute for each other). In the same way, Al and Ti are strongly (anti)correlated (V4). Finally, V2 and V3 are highly correlated to the Fe and Cr contents in nominal compositions, respectively.

Thus, the choice to represent our dataset with a 2-D plot using V1 (along the direction for which [Ni] + [Co] is fixed) and V4 (along [Al] + [Ti] = constant) will give an accurate visualization of the dataset as it will account for 84,9% of the total variance (table S1). V2 and V3 are considered in the 2-D plot with the substitution Co and Ni by Cr and Fe (figure 4c).

3. Additional figures

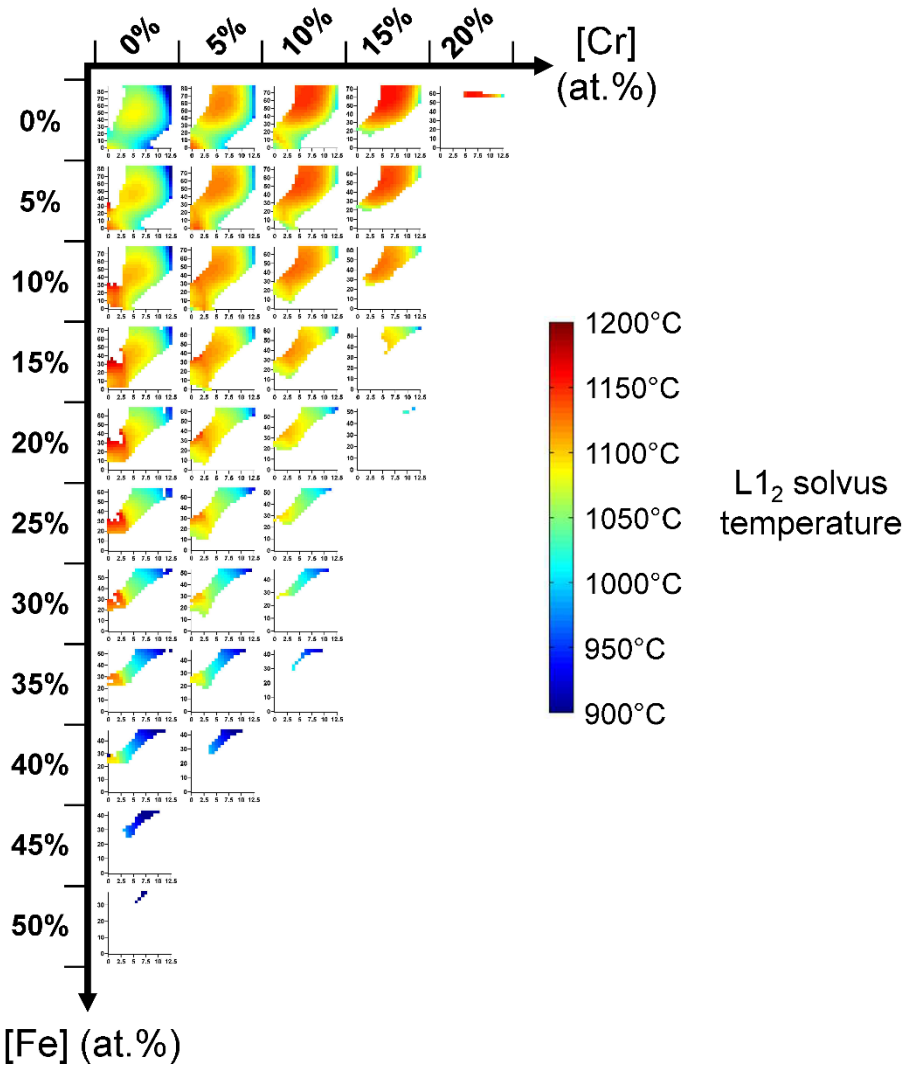

Figure S2: Representation of the $L1_2$ solvus temperature for all alloy compositions with FCC+$L1_2$ microstructures ([Al] + [Ti] = 12.5 at.%) at both 800°C and 1000°C.

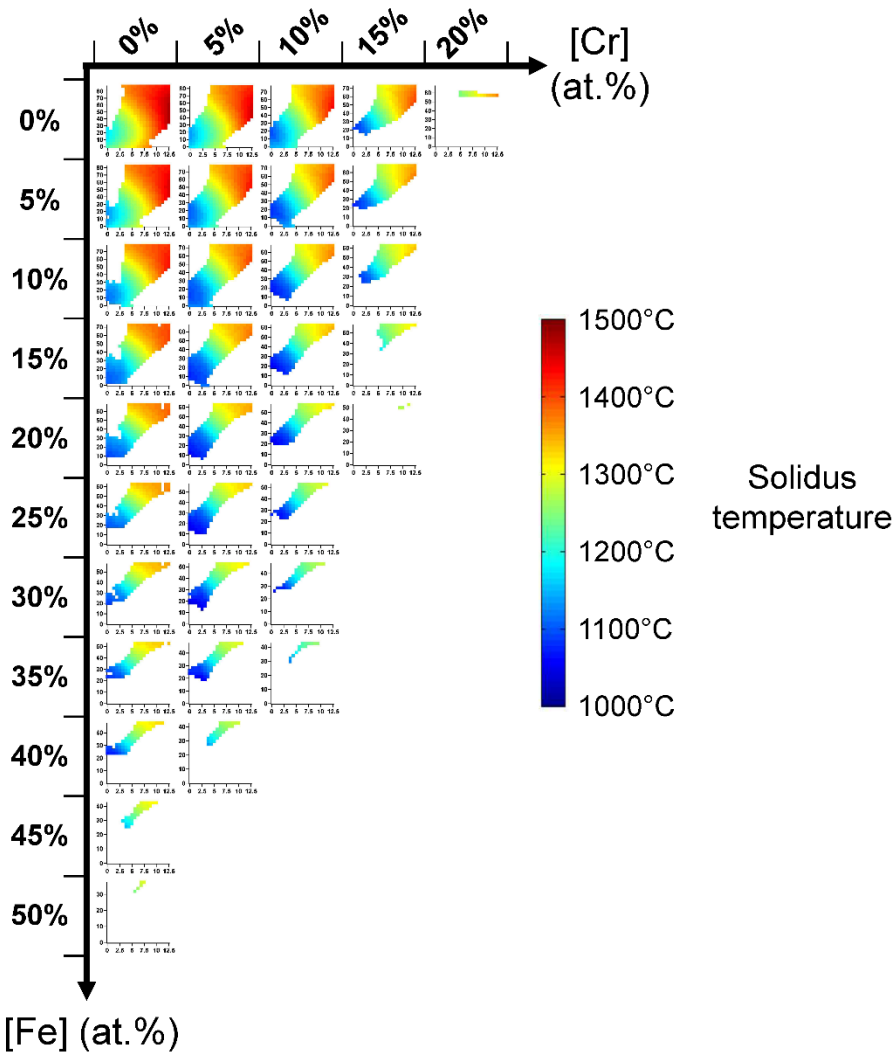

Figure S3: Representation of the $L1_2$ solidus temperature for all alloy compositions with FCC+$L1_2$ microstructures ([Al] + [Ti] = 12.5 at.%) at both 800°C and 1000°C.

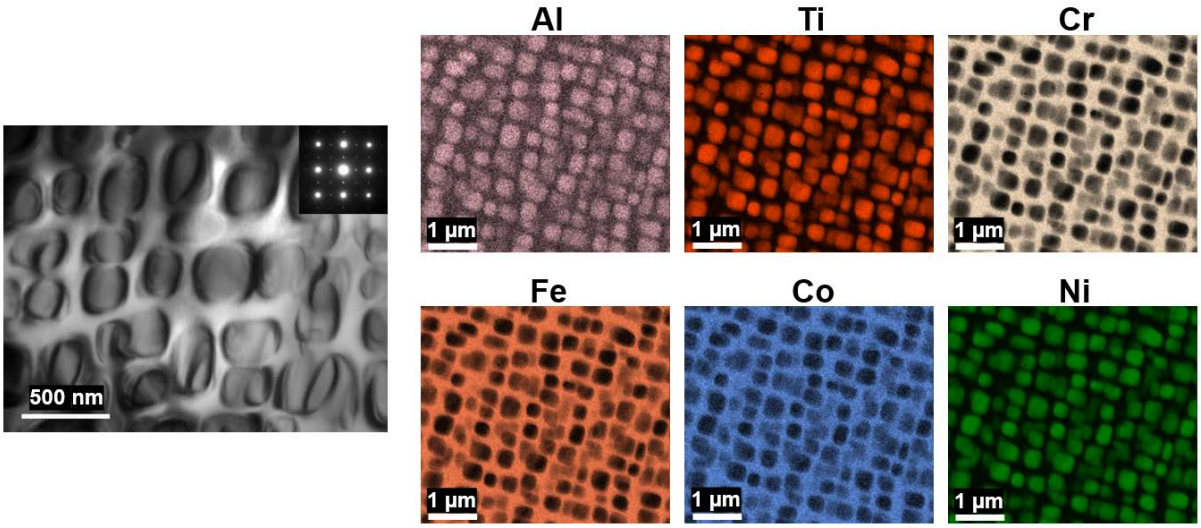

Figure S4: bright-field TEM and STEM-EDX elemental mapping of the TA5 alloy after 1150°C/48h + 900°C/403h heat treatment

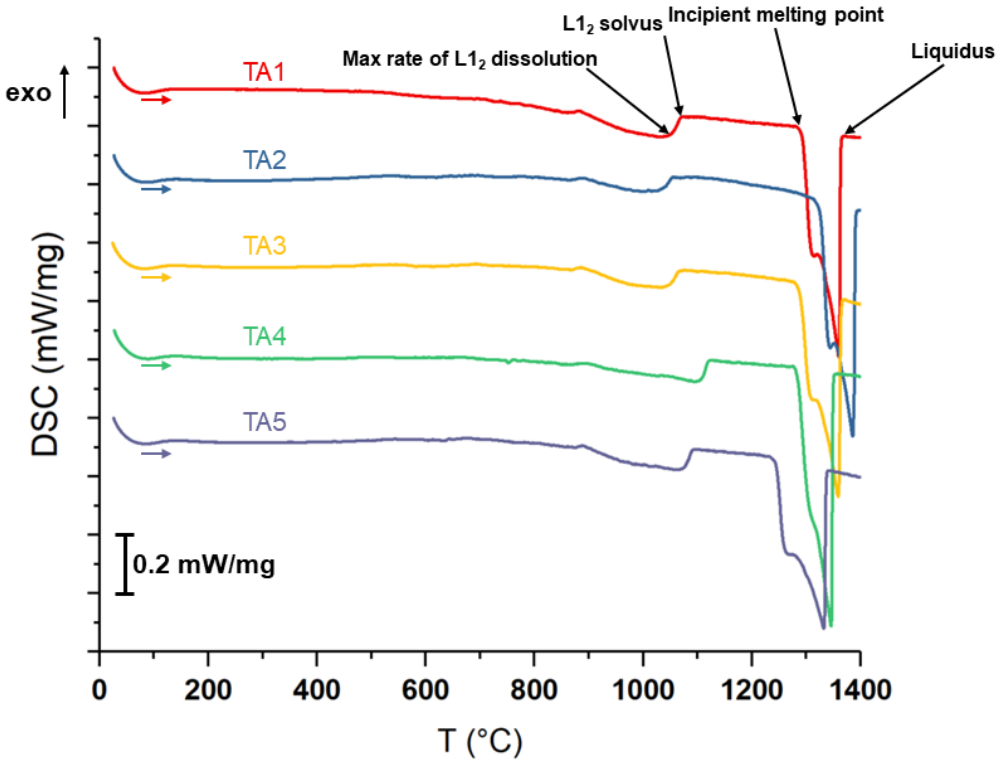

Figure S5: DSC heating curves from room temperature up to 1400°C with a heating rate of 10°C/min for TA1 to TA5 after 1150°C/48h + 900°C/403h heat treatment

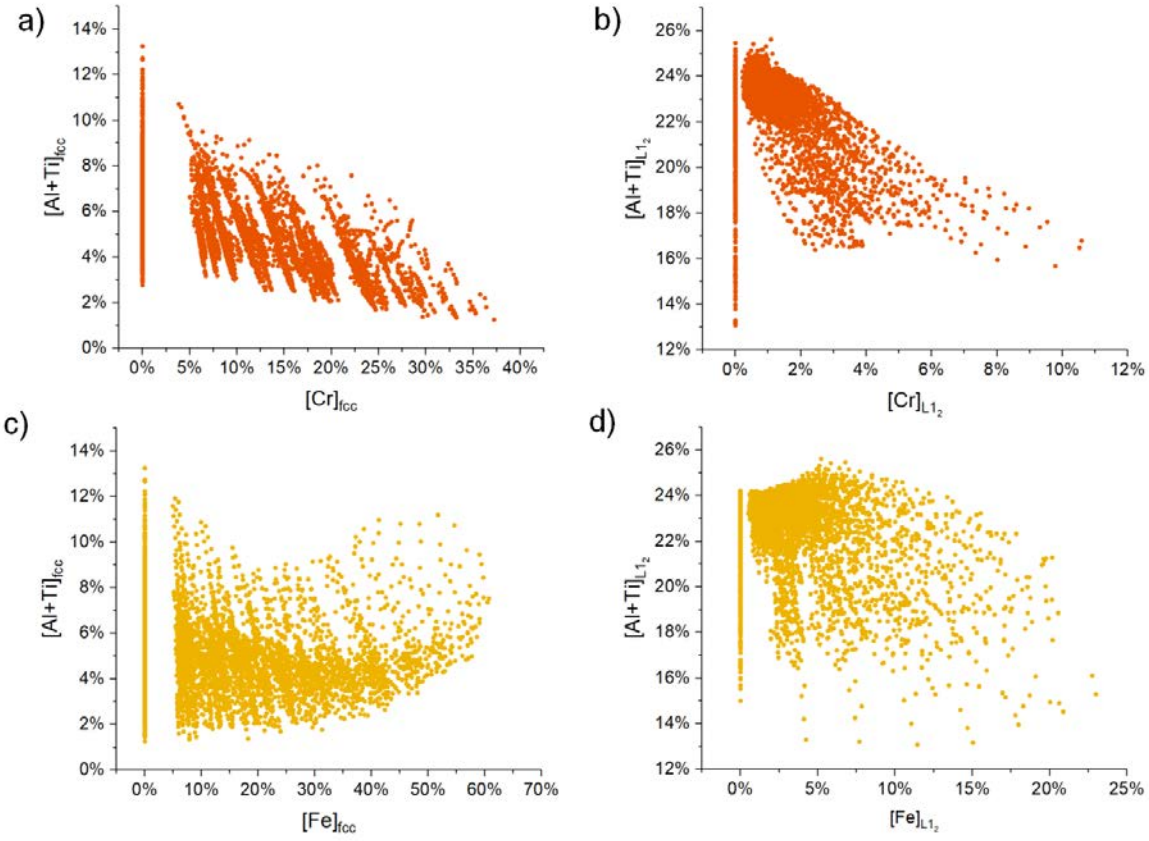

Figure S6: Scatter plot of the 4 562 FCC+$L1_2$ alloys depicting the impact of Cr (a,b) and Fe (c,d) on the solubility of the (Al,Ti) group in the FCC (a,c) and the $L1_2$ (b,d) phases at 800°C.

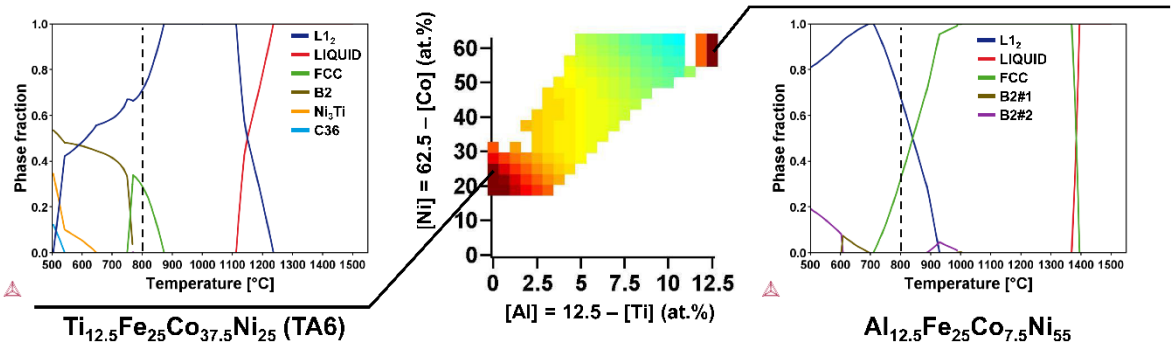

Figure S7: Phase diagram section for [Cr] = 0 at.% and [Fe] = 25 at.% (see fig. 4c). Evolutions of the phase fraction with temperature for two alloy compositions of the section are shown (left and right). Two unexpected features are pointed out in the discussion.

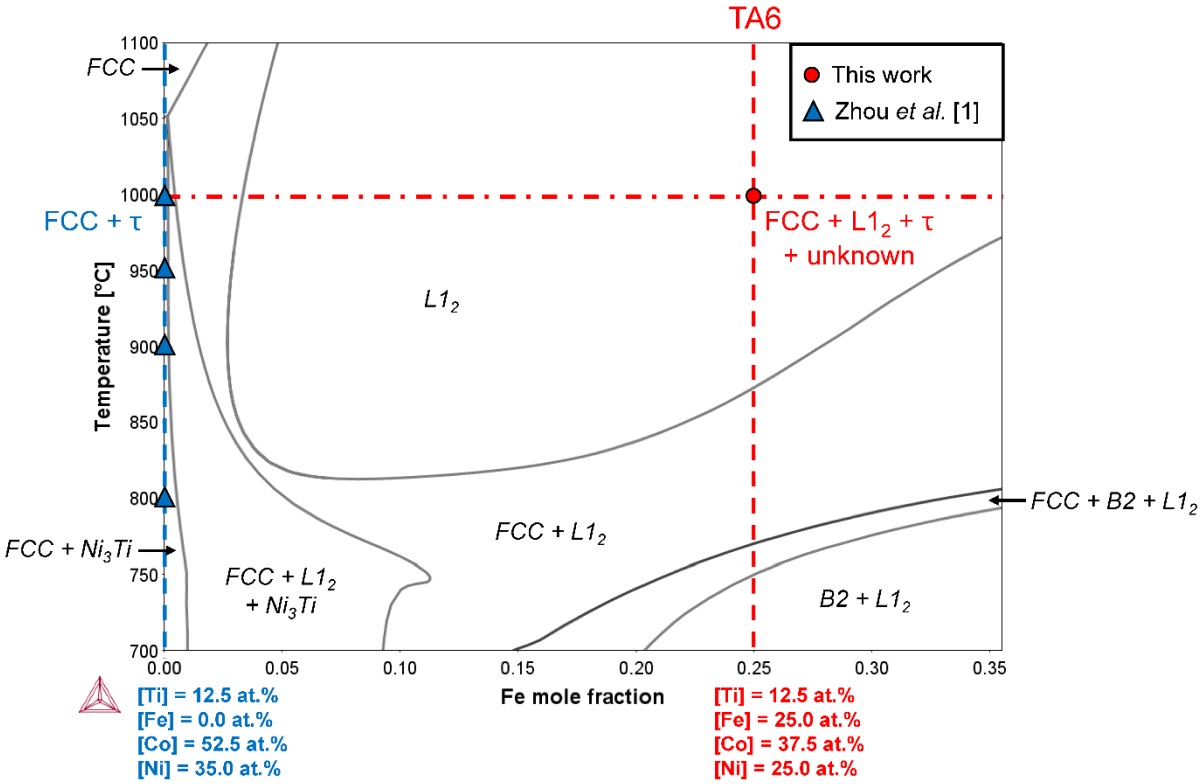

Figure S8: Isopleth calculated in the Co-Fe-Ni-Ti quaternary system for [Ti] = 12.5 at.%, $\frac{[Co]}{[Ni]} = 1.5$, and varying Fe fraction (TCHEA3 database). Experimental data (this work) and past reported results [1] are superimposed.

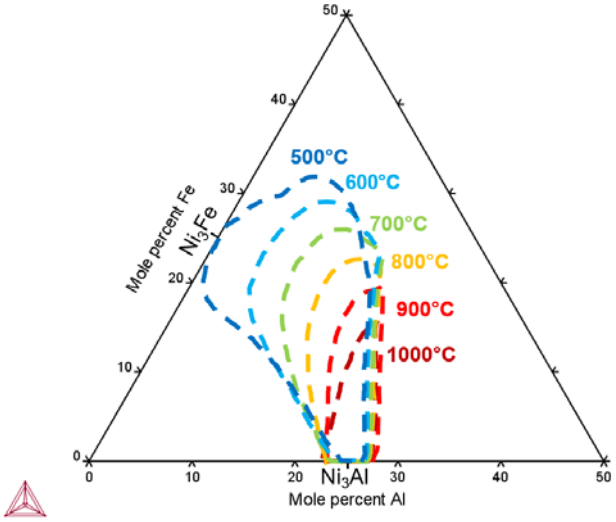

Figure S9: Ni corner of the Al-Fe-Ni ternary phase diagram showing the extent of the L1$_2$ phase field (dashed lines) for temperatures ranging from 500°C to 1000°C. With decreasing temperature, the Ni$_3$Al field grows toward Ni$_3$Fe until complete solubility at 500°C

Reference

[1] C. Zhou, C. Guo, C. Li, Z. Du, Experimental determination and thermodynamic assessment of the Co–Ni–Ti system, Calphad. 63 (2018) 61–76. https://doi.org/10.1016/j.calphad.2018.08.011.